Geophysical transect reveals seismic P-wave velocity structure of the northern Hikurangi margin, New Zealand

Thomas W. Luckie[1], David A. Okaya[1], Katrina M. Jacobs[2], Stuart A. Henrys[2], Andrew C. Gase[3,4], Dan Bassett[2], Harm J. A. Van Avendonk[3], Malcolm White[5], Daniel H. N. Barker[2], Nathan L. Bangs[3], Shuichi Kodaira[6], Ryuta Arai[6], Gou Fujie[6], Yojiro Yamamoto[6]

[1] Department of Earth Sciences, University of Southern California, Los Angeles, CA, USA
[2] GNS Science, Lower Hutt, New Zealand
[3] Institute for Geophysics, Jackson School of Geosciences, University of Texas at Austin, Austin, TX, USA
[4] Geology Department, Western Washington University, Bellingham, WA, USA
[5] Department of Earth, Atmosphere and Planetary Sciences, Massachusetts Institute of Technology, Cambridge, MA, USA
[6] Research Institute for Marine Geodynamics, Japan Agency for Marine-Earth Science and Technology, Yokohama, Japan

Corresponding author: Thomas W. Luckie (luckie@usc.edu)

Key Points

- Combined active- and passive-source tomography reveals the crustal structure of the northern Hikurangi margin
- Reflection and velocity information suggest the presence of underplated sediments beneath the northern Axial Ranges, potentially driving uplift of the forearc
- Velocities help constrain the depth and lateral extent of basement lithologies beneath the northern Hikurangi margin

Abstract

Most conceptual models for how fluids and sediment influence slip behavior and uplift along subduction margins are poorly constrained by geophysical observations. Given the complexity of subduction systems, overcoming this gap in knowledge will require a systems-level approach which uses high quality geophysical constraints. We present wide-angle, onshore-offshore seismic data collected along the northern Hikurangi margin, New Zealand, from which P-wave velocities were calculated using active- and passive-sources. A gravity model and reflection profiles were also assembled to create a complete, ~400 km long transect which images the incoming plate, down going slab, overthrusting forearc, and backarc rift. Velocities and gravity modelling help to constrain the lithology of the forearc basement to ~20 km depth. Upper plate lower crustal velocities and reflectivity point to the presence of underplated sediments immediately above the lithospheric mantle nose, suggesting that underplated sediments are driving uplift of the forearc. Comparing these results to geophysical images from the southern Hikurangi margin, we suggest that the backarc rift influences along-strike changes in the compressional stresses experienced by the forearc, driving changes in bending stresses within the subducting slab.

1 Introduction

Subduction margins exhibit a spectrum of slip rates that bridges stick-slip and stable sliding along megathrusts. Variations in the characteristics of the subducting and overriding plates such as lithology and fluid distribution have been shown individually, through comparative approaches, to influence megathrust behavior (Tichelaar and Ruff, 1993; Oleskevich et al., 1999; Wang and Bilek, 2014). But these parameters cannot fully explain subduction margin megathrust behavior on their own. As a result, we only have a basic understanding of the connections between plate interface slip behavior, upper crustal properties, solid and fluid mass fluxes, and manifestations of plate boundary mechanics and how these can influence processes such as forearc uplift, sediment transfer, and underplating. Feedbacks between multiple geological processes must be considered to fully understand subduction margins at the system level. To overcome this gap in our knowledge, we need high-quality physical and mechanical constraints on the characteristics of subduction margins.

The northern Hikurangi margin offshore North Island, New Zealand (Figure 1) is an ideal candidate to geophysically study a subduction zone. Most of the forearc is subaerial and the subduction interface is relatively shallow. Additionally, previously observed along strike variations between the northern and southern Hikurangi margin (Figure 1), offers the opportunity to investigate controls on stick-slip and aseismic slip. Geodetic studies show along-strike variations from a stick-slip dominated margin in the southern Hikurangi to aseismic creep in the northern Hikurangi (e.g., Wallace et al., 2004, 2009, 2012; Wallace and Beavan, 2010; Lamb and Smith, 2013). The northern Hikurangi Margin hosts backarc extension in the Taupo Volcanic Zone (TVZ) while no arc or backarc is present in the south (Wilson et al., 1995; Wallace et al., 2004; Figure 1), resulting in the northern Hikurangi forearc experiencing a combination of

subduction- and rift-related stresses while the southern Hikurangi forearc only experiences subduction-related stresses. The northern Hikurangi interface is characterized by low interseismic coupling, shallow SSEs, shallow tectonic erosion, thinner sediments overlying the incoming plate, a high number of seamounts, and a high rate of convergence compared to the south (Wallace, 2012, 2020). The northern segment has a history of tsunamigenic megathrust events and hosts more frequent M>5 earthquakes than the southern Hikurangi (Doser & Webb, 2003; Warren-Smith et al., 2017; Wallace et al., 2020). The plate interface has variable dip (Barker et al., 2009; Williams et al., 2013) with local underlying regions displaying high seismic reflectivity (Bell et al., 2010), low resistivity (Heise et al., 2017; Chesley et al., 2021), and high attenuation (Nakai et al., 2021), which point to the presence of fluid rich sediments.

Numerous previous studies have focused on the Hikurangi Margin. The margin was a primary focus site for MARGINS (2000-2009) and its successor program GeoPRISMS (2010-2021), which provided a wealth of information on the offshore Hikurangi setting. This has led to several recent additional studies of the northern Hikurangi performed in the last several years which have primarily focused on slow slip events and plate interface processes (e.g., Wallace, 2020; Yarce et al., 2021; Chesley et al., 2021; Arnulf et al., 2021; Gase et al., 2022; Shreedharan et al., 2022) that have suggested the important role upper plate structure may have on fluid flux, potentially from the mantle (Reyes et al., 2022), and its control on SSE occurrence and distribution.

Underplated sediments accreted beneath the upper plate have been hypothesized to be a driving mechanism for uplift along the forearc in the northern Hikurangi (Walcott, 1984; Wilson, et al., 2007; Figure 1). Wide-angle active source transects from the Seismic Array Hikurangi Experiment (SAHKE; Henrys et al., 2013) in the southern Hikurangi, the North Island Geophysical Transect (NIGHT; Henrys et al., 2003; Henrys et al., 2006) in the central Hikurangi, and the Marine Geoscientific Investigations on the Input and Output of the Kermadec subduction zone (MANGO; Flueh and Kopp, 2007; Scherwath et al., 2010; Bassett et al., 2016) and the RAU07 (Bassett et al., 2010) experiments from the offshore northern Hikurangi all revealed low velocities in the lower Australian crust, with SAHKE also showing prominent lower-crustal reflectivity. These observations have been interpreted as underplated sediments which are correlated with uplift of the Axial Ranges (Nicol & Beavan, 2003; Litchfield et al., 2007; Sutherland et al., 2009) and the offshore East Cape Ridge (Scherwath et al., 2010). Highly conductive (< 20 Ωm) features near the base of the Australian crust in the northern Hikurangi have also been interpreted as underplated sediments (Heise et al., 2017), however there has previously been no direct geophysical imaging of these anomalies beneath the onshore northern Hikurangi. Confirming the hypothesized presence of underplated sediments beneath the Raukumara Peninsula (Litchfield et al., 2007; Wallace et al., 2009) would further support the role sediments play in uplift along the entire North Island. On a broader scale, understanding both the structure, properties, and potential lithology of the upper plate is key to understanding the overall behavior of the northern Hikurangi margin.

Little is known about the basement beneath the northern Hikurangi Margin forearc and the extent of mapped onshore geologic units beneath the Raukumara Peninsula (Mazengarb & Speden 2000), but evidence suggests these units may play an important role as a mechanical backstop along the margin. Offshore seismic data have revealed a narrow (~30 km) accretionary prism in front of a deforming backstop composed of passive margin sedimentary units which extends at least ~65 km inboard of the trench (Barnes et al., 2010; Gase et al., 2021; Figure 2). Seismic reflection profiles from the southern Hikurangi suggest that the inner prism is composed of the Cretaceous-aged Torlesse Supergroup (Bland et al., 2015). In the northern Hikurangi, Gase et al. (2021) suggests a mechanical boundary between the deformed backstop and the frontal prism as interpreted from seismic velocity and reflection profiles. Bangs et al. (2023) suggest this offshore boundary is due to a past seamount collision. Deformation in the northern Hikurangi ceases between the east coast and ~20 km inland beneath the Raukumara Peninsula (Mountjoy & Barnes et al., 2011). However, the nature of the backstop farther inboard and onshore in the northern segment remains uncertain and the possible role that the Torlesse may play as a more competent, possibly rigid backstop in the northern Hikurangi remains to be seen. Shallow slow slip along the margin is focused updip of the Torlesse, suggesting that the Torlesse may also influence the location of the shallow frictional transitions along the subduction interface (Bassett et al., 2022). This gap in our understanding of the inboard backstop in the Northern Hikurangi means that the role of onshore geologic units and structure in the northern Hikurangi and its connection to the interpreted offshore backstop remains undetermined. Unraveling the possible role of the Torlesse as a backstop is predicated on first understanding the distribution of the Torlesse in the Raukumara Peninsula basement.

In this study we present a ~400 km long transect across the northern Hikurangi subduction margin that captures the incoming Pacific oceanic crust, forearc accretionary prism, down going Pacific slab, overriding Australian continental crust, and backarc rift. This transect includes (1) P-wave velocities (Vp) calculated from active and passive source travel time data collected by the Seismogenesis at Hikurangi Integrated Research Experiment (SHIRE) project, (2) a free air gravity anomaly profile, and (3) offshore multichannel seismic (MCS) data and onshore single-fold common depth point (CDP) stacks that provide a reflectivity model which directly images intracrustal boundaries along the transect. A segment of the SHIRE transect imaging the frontal accretionary prism presented by Gase et al., (2021) identified a deformed inner prism with high seismic velocities and an accretionary prism segmented by a network of thrust faults. Gase et al. (2019) imaged the backarc TVZ, which revealed a thinning crust across the rift and evidence for magmatic instructions in the middle and lower crust. With the complete SHIRE transect presented here, we image the forearc across the coastline as well as the plate boundary beneath North Island to better understand the structure and lithology of the northern Hikurangi and provide along strike comparisons to previous seismic surveys conducted along the southern section of the Hikurangi margin to gain insight into the overall crustal structure and nature of the entire margin.

2 Hikurangi tectonic setting

The Hikurangi Trough extends along the eastern coast of North Island and is a result of the Pacific Plate subducting westward beneath the continental Australian Plate (Figure 1). Subduction along the Hikurangi Margin began ca 27-30 Ma (van de Lagemaat et al., 2022) with a current subduction rate of 60 mm/yr in the north to 22 mm/yr in the south (Wallace et al., 2004). Along the northern Hikurangi margin, near the Raukumara Peninsula, there is ~40 mm/yr of plate motion (Nicol & Beavan 2003; Wallace et al., 2004). The northern Hikurangi margin is characterized by a narrower offshore forearc with a poorly developed frontal prism with widespread evidence of seamount collisions (Gase et al., 2021; Figures 1, 2). Arc volcanism and backarc rifting of the TVZ extends offshore in the Bay of Plenty (Figure 1).

2.1 Incoming Pacific Plate

The incoming Pacific Plate in this area includes the Hikurangi Plateau (Figure 1), a ~7-11 km thick (Mochizuki et al., 2019; Gase et al., 2021) Cretaceous-aged large igneous province (LIP) and is what remains of the larger Ontong-Java-Manihiki-Hikurangi LIP (Wood & Davy, 1994; Taylor 2006; Davy et al., 2008). The Hikurangi Plateau separated from the larger LIP sometime after 115 Ma (Kroenke et al., 2004; Mortimer et al., 2006). Portions of the basement of the Hikurangi Plateau have been dated to 96-118 Ma, indicating volcanism continued after the Ontong-Java-Manihiki-Hikurangi LIP broke up, with volcanism continuing until recently (Hoernle et al., 2010). The Hikurangi Plateau is ~8-11 thick in the northern Hikurangi and is characterized by rough bathymetry composed of numerous seamounts and porous volcaniclastic sediments atop an oceanic basement (Barnes et al., 2020; Gase et al., 2021; Bassett et al., 2022; Figure 1). On average, there are 1-2 km thick sediments on the Hikurangi Plateau, covering a seismically reflective, high relief volcaniclastic basement which can vary by several hundred meters (Gase et al., 2021). The accretionary wedge thickness generally decreases from south to north along the Hikurangi, correlating with the decrease in sediment thickness on the incoming plate (Fagereng, 2011). Seismic velocities in the Pacific mantle calculated by Mochizuki et al. (2021) reveal $V_p > 8.0$ km/s and localized regions of $V_p/V_s > 1.8$ near dense areas of faulting crossing the Moho. These were interpreted as regions of high fluid content, with faults acting as conduits for fluid migration from the mantle into the Pacific Plate (Mochizuki et al., 2021), with the Pacific mantle experiencing a low degree (<10%) of serpentinization (Grevemeyer et al., 2018; Gase et al., 2021)

2.2 Plate interface

The plate interface, as inferred by Williams et al. (2013) using MCS observations, earthquake hypocenters, and regional tomography models, displays a northwest dipping interface and variations in dip with a wavelength of 10s of km, increasing from a dip of ~7° near the trench to ~20° near the intersection with the Australian Moho. Finer scale imaging of the plate interface beneath the eastern Raukumara Peninsula from receiver functions showed a plate roughness on the scale of 1s of km, interpreted as volcanic sediments and/or seamounts, which

leads to a variability of shear-strength along the plate interface (Leah et al., 2022). Marine multichannel seismic data from Gase et al. (2021) imaged a rough subducting plate, with volcaniclastic sediments producing strong reflectivity and contributing to geometric roughness near the decollement.

The northern Hikurangi interface hosts shallow SSEs, whereas the southern Hikurangi hosts deeper SSEs (Wallace et al., 2004; Figure 1). An offshore SSE in late 2014 was recorded by the Hikurangi Ocean Bottom Investigation of Tremor and Slow Slip (HOBITSS) experiment (Wallace et al., 2016; Zal et al., 2020; Figure 1). During this event, Zal et al. (2020) observed an increase in Vp/Vs ratios and shear wave splitting delay times, which were interpreted as fluid movement during rupture of the SSE patch. Additionally, Yarce et al. (2019) assembled a seismic catalog using HOBITSS data which revealed a microseismicity gap at the downdip limit of the late 2014 SSE and correlates with a local increase in interseismic coupling (Wallace et al., 2016). Vertical streaks of seismicity in the slab below the SSE region and an increase in heat flow have been interpreted as related stress-generated bending faults that enable the migration of fluids and which increases pore fluid pressure on the interface, driving SSEs (Wallace et al., 2016; Warren-Smith et al., 2019; Yarce et al., 2019). High Vp and Vp/Vs in the Pacific slab and upper mantle support the interpretation of the presence of fluids (Mochizuki et al., 2021; Yarce et al., 2021). Heat flow measurements landward of the deformation front point to advective fluid flow along faults within the slab, consistent with the conclusion that slow slip is enabled by high pore fluid pressures (Antriasian et al., 2018). These results underscore the complexity of plate interface and intraslab processes occurring in the shallow portions of the margin and highlight the importance of high-resolution velocity measurements to constrain the distribution of fluids.

Five IODP sites were drilled in two expeditions in the northern Hikurangi to further investigate fluids in the upper plate (Barnes et al., 2019; Saffer et al., 2019), including site U1520 which sampled sediments from the Hikurangi trough (Figure 2). Site U1518 (Figure 2) sampled a megathrust splay fault which exhibited strong ductile deformation in the footwall, with brittle deformation observed in the hanging wall. This has been interpreted as the result of seafloor overthrusting which formed a low-permeability seal, driving high pore fluid pressures in the footwall (Morgan et al., 2022). Such a setting could facilitate the occurrence of SSEs on the megathrust (Wallace et al., 2016; Morgan et al., 2022). Understanding the upper plate structure and fluid migration across the entire Hikurangi subduction system is fundamental to better understand how and why SSEs occur in this region and may shed light on controls on plate interface locking.

2.3 Overlying Australian Plate

Onshore, the geology of the Raukumara Peninsula can be divided into eastern and western halves (Figure 2). The eastern Raukumara Peninsula is composed of primarily Neogene-aged marine sediments deposited after the initiation of current Hikurangi subduction (Rait et al., 1991; Sutherland et al., 2009). Near the center of the Raukumara Peninsula, early Cretaceous to Oligocene sedimentary rocks deposited in a marine environment, comprising part of the East Coast Allochthon (ECA), are present at the surface (Mazengarb & Speden, 2000; Crampton et

al., 2019). The ECA units are calcareous mudstones emplaced during subduction initiation of the Hikurangi Margin 27-30 Ma (Mazengarb & Speden, 2000; van de Lagemaat et al., 2022) and have been transported 10s to 100s of km to the southwest along low angle detachment faults (Rait et al., 1991; Mazengarb & Speden, 2000; Sutherland et al., 2009). These allochthonous units dip eastward and underlay the Neogene units at a depth of ~3 km, as constrained by seismic data (Mazengarb & Speden, 2000). The offshore extent of the Neogene and ECA units in this region and the basement below the eastern Raukumara Peninsula remains unconstrained (Mazengarb & Speden, 2000; Crampton et al., 2019). The basement of the western Raukumara Peninsula is composed of the Pahau Terrane, part of the Torlesse Composite Terrane, a Cretaceous-aged graywacke which was deposited during active Gondwana margin subduction (Mazengarb & Speden, 2000; Sutherland et al., 2009; Crampton et al., 2019). The offshore extent of the Torlesse in the northern Hikurangi remains relatively unconstrained. Using wide-angle seismic and MCS data, Bassett et al. (2022) propose the Torlesse extends beneath Hawke Bay, while limited onshore seismic data suggests the Torlesse extends to at least ~5 km depth, underlying the ECA in the eastern Raukumara Peninsula (Mazengarb & Speden, 2000).

2.4 TVZ backarc rift

The TVZ is a 300 km extensional arc running parallel to the Hikurangi subduction zone from central North Island to the Bay of Plenty (Figure 1) experiencing intra-arc rifting at a rate of ~15 mm/yr near the Bay of Plenty (Wallace et al., 2004). Volcanism in the TVZ initiated ~21 Ma (Wilson et al., 1995) with the Bay of Plenty opening ~10 Ma (Lamarche et al., 2006). The most recent stage of volcanism in the TVZ occurred from 0.34 Ma to present (Brothers et al., 1984; Wilson et al., 1995). In addition to volcanism, the TVZ also hosts trench perpendicular backarc extension at a rate of 12-15 mm/yr in the Bay of Plenty (Wallace et al., 2004). Grabens in the TVZ display oblique rifting with active listric normal faults with blocks tilted by 12-16° (Davey et al., 1995; Lamarche et al., 2006). Seismic velocities interpreted by Gase et al. (2019) point to higher magma flux near the eastern shoulder of the TVZ in the Bay of Plenty, with reflectivity profiles suggesting intrusions and sills in the mid crust.

3 The SHIRE project

3.1 Overview

From 2017 through 2019, the multinational and multidisciplinary SHIRE project collected data along the Hikurangi margin, North Island, New Zealand (Figures 1, 2) with the goal to investigate the feedbacks between subducting plate interface slip behavior, solid and fluid fluxes, and long-term plate-boundary mechanics uncovering the driving processes connecting forearc uplift, sediment transport and underplating, plate-boundary strength, and seismogenesis (Bangs et al., 2018; Barker et al., 2019; Jacobs et al., 2020).

The project had three disciplinary components; paleoseismological investigations of deformation, numerical modelling, and geophysical imaging. (1) The paleoseismology component helped to resolve the megathrust slip behavior over many seismic cycles to constrain long-term coastal uplift and subsidence patterns along the margin (e.g., McKinney et al., 2018;

Hamel et al., 2019). (2) The geodynamical modelling component used the SHIRE data with existing geophysical and geological data to constrain models of the physical state of the interface and the evolution of the margin over both long and short timescales by modelling subduction and plate interface properties (e.g., Sun et al., 2020). It also sought to quantify links between in situ conditions, fluid flow, subduction thrust behavior, and development of the subduction margin by testing the influence of sediments and fluids on the subduction system. (3) The geophysical imaging component involved an active-source onshore-offshore seismic survey conducted from trench to backarc in two field campaigns to assess the physical mechanisms that control slip behavior and uplift of the northern Hikurangi margin (Bangs et al., 2018; Barker et al., 2019; Jacobs et al., 2020; Figures 1, 2). In this study we present results from the SHIRE wide-angle seismic survey by performing travel time tomography to invert for a 2-D P-wave velocity structure along the northern Hikurangi margin and compare these results to the SAHKE geophysical transect to investigate controls and influences on the observed along strike variations of the Hikurangi margin.

3.2 Seismic transects

The geophysical imaging component of SHIRE involved an active-source onshore-offshore seismic survey that collected both wide-angle and MCS data, conducted from trench to backarc in two phases to assess the physical mechanisms that control slip behavior and uplift of the northern Hikurangi margin (Figures 1, 2). SHIRE collected four main geophysical transects: two trench-perpendicular and two trench-parallel, covering the entire Hikurangi Margin (Figure 1). This rich dataset permits the 2-D seismic imaging of the entirety of the Hikurangi subduction margin: the incoming oceanic plate, accretionary prism, subduction interface, overriding crust, mantle wedge, and backarc. Transect 1 (T1), which we utilize in this study, is WNW-ESE trending, ~400 km long and spanned the entire along-dip expanse of the subduction margin from incoming plate to backarc (Figure 2). T1 included a ~4 month onshore-offshore phase of SHIRE (OBS, MCS, and onshore instruments recording airgun shots) and a ~2 month onshore-only phase of SHIRE (onshore instruments recording explosion sources). The primary goals of T1 were to calculate a seismic velocity and reflectivity image of the incoming oceanic plate, accretionary prism, subduction interface, overriding crust, mantle wedge, and backarc. In addition to T1, Transect 2 (Mochizuki et al., 2019) is a complementary ~170 km long trench-perpendicular line in the southern Hikurangi, with the goal of collecting additional offshore data to extend the existing double-sided SAHKE onshore-offshore transect examined by Henrys et al. (2013). Transect 3 is a ~490 km long trench parallel line which sought to examine along-strike variations in the crustal structure of the forearc, underthrusting crust, and sediments (Bassett et al., 2022). Transect 4 is a ~450 km long trench parallel line but had the goal of examining the structure of the incoming plate prior to subduction.

The offshore survey phase, SHIRE Phase I, was carried out from October 2017 to February 2018 and included an onshore array which recorded offshore sources. Using the *R/V Langseth*, Phase I of SHIRE acquired 5,489 km of marine seismic reflection and refraction data

along the entire east coast of North Island, New Zealand, as well as the Bay of Plenty. This includes 1,443 km of wide-angle ocean bottom seismometer (OBS) data along the four major transects (Figure 1). A total of 210 OBS instrument sites spaced ~10 km were deployed by the *R/V Tangaroa* to record airgun shots, spaced 150 m, from the *R/V Langseth*. In addition to the OBS data, 89 onshore seismometers were deployed across the Raukumara Peninsula to supplement the northern OBS transect and record onshore-offshore (OO) arrivals (Figures 1, 2). Forty-six of these OO stations were deployed in a linear array and spaced ~2 km apart and recorded data continuously for 4 months. In addition to this wide-angle OBS data, 4,046 km of multichannel seismic (MCS) data were collected. The MCS profiles used the same seismic source as the OBS instruments but were spaced every 50 or 35 m. T1 MCS profiles were collected in the Bay of Plenty (MC 03; Figure 2) and the Pacific Ocean (MC 10; Figure 2).

The onshore survey phase, SHIRE Phase II, was focused along T1 and conducted between February and March 2019. Phase II of SHIRE involved deploying 583 geophones along T1 at an average spacing of 150 m in a ~90 km linear array across the Raukumara peninsula (Figure 2). Every second station deployed recorded 3-component seismic data; the remaining stations recorded only vertical-component data. Additionally, 19 continuous short period stations were deployed off the transect to provide 2-D coverage in the array. In total, these instruments were deployed for two weeks and geophones recorded data in eight 4-hour windows around potential shot windows. The sources recorded by these instruments were five 500 kg explosive sources placed at 50 m depth (Figure 2).

4 Travel-time tomography method

Manually picked wide-angle seismic phases were used in the 2.5-D travel-time tomography approach of Van Avendonk et al. (2004) to estimate the 2-D P-wave velocity structure of T1. Ray tracing was performed in 3-D to account for irregular, crooked source-receiver geometries of +/-8 km out of plane. The model perturbations were then inverted in 2-D. The 2-D starting model was constructed by laterally averaging the velocities from a regional 3-D model (Eberhart-Philips, 2020). The tomographic model was constructed in two steps to alleviate vertical smearing of travel time misfits: First by inverting for first arrivals, then subsequently incorporating layer boundaries and secondary phases. The OO picks were decimated by a factor of 3 to match the airgun spacing of the OBS data. The plate interface boundary (Williams et al., 2013) was inserted after the first-arrival inversion. The Pacific Moho was inserted by adjusting the Williams et al. (2013) boundary to reproduce the Moho depth reported by SLAB 1.0 (Hayes et al., 2012). Finally, the Australian Moho depth was taken from Gase et al. (2019) to complete the layered model. Velocities below the Moho in the first-arrival model were set to linearly increase from 8.0 km/s at the Moho to 8.5 km/s at a depth of 60 km to prevent tunneling of deeper turning refracted phases. After these modifications, deeper turning refracted and reflected phases were incorporated.

Due to the large amount of continuous data recorded during the SHIRE project in a highly seismically active region, earthquakes in the data were identified and located using the

coalescence method of the opensource software QuakeMigrate (Smith et al., 2020; Figure 3). Events within +/-10 km of T1 with location errors <2 km were used in the inversion. Picks from the location method were combined with the active source picks to improve the spatial distribution of sources and raypaths though the model, providing additional constraints on velocities in the middle- and lower-Australian crust, Pacific slab, and Australian and Pacific mantles. Picks from 178 events were added to the inversion (Table S1) to produce the final velocity model presented here. Local magnitudes for these events ranged from 0.63 to 2.71, with a mean local magnitude of 1.31, and depths ranged from ~0.1 km to 46 km. Manually assigned pick uncertainties ranged from 17 ms to 250 ms with a mean uncertainty of 104 ms.

This final model (Figure 3), constructed from 64,276 picks (Table S2 in supplementary material), has a χ^2 misfit of 1.11 and a travel-time root mean squared (RMS) error of 184 ms, suggesting that the data agree with the assigned pick uncertainties. Resolution of the model was assessed by the recovery of perturbation ellipses of varying sizes (Van Avendonk et al., 2004; Figure S1). Additionally, velocities and boundary depths were perturbed for the slab interface and slab Moho to estimate model sensitivity and to assess depth errors for these boundaries (Figure S1 and supplementary material), where perturbed models with a $\chi^2 < 1.25$ were considered acceptable.

5 Results

5.1 Reflection profiles

Single-fold common depth point (CDP) stacks using precritical reflections from the land explosion gathers were constructed to provide insight into the reflectivity of the onshore portion of T1 (Figure 3A). By pairing it with the offshore Pacific and Bay of Plenty MCS data, we can construct a nearly complete ~400 km long reflection profile. This provides insights into reflectivity of the lower crust beneath the Raukumara Peninsula and helps to connect observations and interpretations from the Pacific and Bay of Plenty MCS profiles.

MCS reflection imaging processing was carried out by Gase et al. (2019; 2021; Figure 3A). In the MC 10 Pacific profile, Gase et al. (2021) revealed a ~3.5 km thick sediment package above a basaltic basement in the incoming Pacific plate with potential underthrusted volcaniclastic lithologies below the megathrust. Reflection imaging interpreted in Gase et al. (2019) from MC 03 in the Bay of Plenty revealed a ~2 km thick layer of sediments above basement in the TVZ. A ~25 km wide region from ~5 to 15 km depth is characterized by chaotic and subparallel reflections, which has been interpreted as recently intruded sills in the mid-crust (Gase et al., 2019; R1 in Figure 3A).

Lower crustal reflections beneath the Raukumara Peninsula immediately above the Australian Moho at ~27 km depth are observed in the CDP stack (R2 in Figure 3A and 4. This zone of reflectivity is ~4 sec TWT thick (~10 km) and laterally continuous for ~65 km, from the Moho intersection with the plate interface to the west coast of the peninsula. Similar reflections have been observed in the southern Hikurangi (Henrys et al., 2013), however, these previously observed reflections in the south are both thinner (~3 sec TWT, ~8 km) and narrower (~35 km)

than the reflectivity seen here. Additionally, the southern reflectivity is observed beneath the Australian crust up dip of the Australian mantle wedge, rather than immediately above the mantle on T1.

5.2 Transect 1 wide-angle data

From the combined SHIRE Phase I and II T1 data, co-located OO receiver and explosion shot gathers can be combined as supergathers (Okaya et al., 2002) which shows laterally coherent wide-angle phases across the entire ~400 km transect (Figure 3B). With such a representation of the data, patterns of many seismic phase arrivals indicative of a subduction zone become apparent, assisting in the interpretation of gathers from the individual acquisition components.

The OO data from the Bay of Plenty shows generally clear crustal refractions (P_{gAus}) on stations deployed on the western half of the Raukumara Peninsula (Figures 3B and S3-S5). This is accompanied by Australian Moho reflections ($P_{mAus}P$) and, with generally lower signal-to-noise ratio, mantle refractions (P_{nAus}; Figure S3). Arrivals from these stations extend to maximum offsets of ~150 km. OO stations deployed on the western half of the peninsula also record clear arrivals from airguns in the Pacific (Figure S4).

Offshore airgun sources near the coast in the Pacific recorded by onshore stations appear to be controlled by a slow velocity structure in the prism (Figure 3B, S4). First arrivals within 20 km offset have apparent velocities of ~3.0 km/s, indicating refractions through seismically slow sediments in the accretionary prism. Beyond 40 km offset, mantle refractions appear, with a typical apparent velocity of ~8.0 km/s and an arrival pattern heavily influenced by seafloor topography (e.g., Figure 3B, S3, S4). Between 20 km and 40 km offset, two phases of note appear: A Pacific Moho reflection ($P_{mPac}P$) and transitionary phase (P_x) between P_{prism} and P_{nPac} (Figure S5) Interestingly, P_x displays an apparent velocity of ~5.0 km/s, indicative of a crustal feature. The slight parabolic moveout of P_x may signal that this is a reflection, although it is difficult to observe any reflection-refraction transition associated with P_x. Such a phase may not add useful information to a travel-time tomographic inversion scheme so was not used in the analysis presented here.

The onshore explosion source gathers record the phases generated by the down-going Pacific Plate and intersection of the Australian Moho and slab interface. The easternmost shot, SP1, (Figure S6) contains clear Australian crustal refraction (P_{gAus}) arrivals across the entire gather, followed by a reflection from the plate interface ($P_{int}P$). The poor signal-to-noise ratio obscures any expected Pacific slab Moho reflection ($P_{mPac}P$)—however, $P_{mPac}P$ as well as $P_{int}P$ does appear in the western portion of the shot SP2 gather (Figure S7). Shot SP3, which is located above the intersection of the Australian Moho and plate interface records $P_{mPac}P$ and $P_{int}P$ quite clearly across all offsets (Figure 3B, S8). This is the first appearance of a reflected phase from the Australian Moho ($P_{mAus}P$) in the onshore explosion data. Shots SP4 and SP5 display these same phases, displaying the expected moveout of $P_{int}P$ and $P_{mPac}P$, given that the slab is deepening to the west (Figure S9, S10). Apparent velocities of P_{gAus} across all shots illustrates

that apparent P_{gAus} velocities tend to be slower in the eastern portion of the gathers, with slightly lower signal-to-noise ratios from these stations.

There is a clear difference in signal-to-noise ratio (SNR) and apparent velocities between the eastern and western portions of the onshore explosion and OO data. High SNR and higher apparent velocities appear in the western third of the Raukumara Peninsula, particularly stations installed on the Cretaceous-aged Torlesse composite terrane (Mazengarb & Speden, 2000; Figures 2, 3B, and supplementary material). In the eastern portion of the onshore arrays, where stations are installed on younger Neogene sedimentary units, both lower SNR and slower apparent velocities are observed (Mazengarb & Speden, 2000; Figures 2, 3B). The SNR difference is most clearly demonstrated by observing airgun-sources in the Pacific arriving at a station deployed near the west coast of the peninsula (Figure 3B, S3)—the converse, Bay of Plenty sources arriving at the east coast, is not observed. Onshore explosion gathers highlight the change in apparent velocities across the peninsula which is correlated with a change from Cretaceous to Neogene units (Figure 3B, S6-S10). This highlights the influence the near surface lithology can have on SNR, apparent velocities, attenuation, and shadow zones wide angle data.

The OBS gathers from the Bay of Plenty show distinct Australian crustal refraction (*Paus*) and Moho reflection ($P_{mAus}P$) arrivals to maximum offsets of ~75 km (Gase et al., 2019; Figure S11). Similar arrivals are seen from the Pacific-side OBSs, with the addition of occasional mantle refractions (P_{nPac}) that extend to maximum offsets of ~90 km (Gase et al., 2021; Figure S12). Gase et al. (2019, 2021) provide additional descriptions of the SHIRE OBS data used in this study.

5.3 Seismic velocity model

The resulting T1 P-wave velocity model has ray coverages to depths of ~45 km beneath the Raukumara Peninsula (Figure 3C). Dense ray coverage, with multiple crossing ray paths, are located to depths of ~10 km in the Bay of Plenty, ~15 km beneath the Raukumara Peninsula, and ~15 km in the Pacific (Figure S1A). Deeper diving rays from the OO data fill in ray coverage to ~45 km, albeit with sparser coverage and less crossing paths. The velocity structure in the marine portions of the transect, originally described in Gase et al. (2019) and Gase et al. (2021), remains generally unchanged. However, improved ray densities from additional OO data and incorporated earthquakes noticeably increases the model coverage, particularly across the coast lines and in the upper mantle. The increased ray coverage and densities from onshore-offshore data, along with the inclusion of a slab boundary in the inversion procedure, creates a more complete tomographic model of T1 and increases the confidence in the velocity structure in these portions of T1 as compared to Gase et al. (2019, 2021).

The velocity model reveals that the incoming Pacific Plate has a ~3 km thick layer of sediments (Vp < 3 km/s) which includes volcaniclastic sediments from the upper Hikurangi Plateau, overlying the ~10 km thick Hikurangi Plateau basement, which exhibits a smooth velocity gradient from 3 km/s to ~7 km/s at the Moho (Figure 3C). The incoming Pacific plate has a total thickness of ~12 km at the trench, thinning to ~8 km beneath the east coast of the

Raukumara Peninsula, with slab dip increasing from ~7° to ~14° over the same segment (Figure 3C). Beneath the center of the Raukumara Peninsula, the slab begins to thicken with depth (Figure 3C). It is possible that changes in slab thickness beneath the Raukumara Peninsula are due to trade-offs occurring within the velocity model calculation. The slab interface boundaries within the velocity model are primarily sampled by rays without reciprocal paths due to the geometry of the slab relative to the source distributions, reducing confidence in the boundary depths (Figure S1A). Plate interface or plate Moho reflections, which would provide the best constraints on boundary geometries, are relative sparse compared to other phases in the model (Figures S1A, S3-S13). Incidentally, Pacific mantle refractions (P_{nPac} phases) provide the highest contribution to ray densities in this portion of the model (Figure S1A) which, while improving resolution of velocities in the mantle, may contribute to velocity-depth trade-offs within and above the slab. Additionally, ray coverage in this region decreases significantly below ~30 km depth (Figure S1), leading to these boundaries being poorly constrained. As a result, we caution any geologic-based interpretation on slab thinning.

A noticeable velocity high immediately east of the trench in the Pacific crust correlates with the location of Puke Knoll, a ~20 by ~3 km seamount (Figure 2, PK in Figure 3C). The Pacific mantle displays a relatively uniform velocity of ~8 km/s outboard of the trench, with slightly slower velocities of ~7.5 km/s beneath the forearc. The accretionary prism displays slow shallow velocities < 2.5 km/s which correlate with the location of several basins, both offshore and onshore. Beneath the inner prism, immediately above the plate interface, a pocket of elevated velocities (>4.5 km/s) is observed (V1 in Figure 3C), which has previously been interpreted as either a geologic boundary or enhanced compression from a past seamount collision (Gase et al., 2021; Bangs et al., 2023).

Onshore, beneath the Raukumara Peninsula, the Australian crust has a thickness of ~27 km. A clear east-west horizontal gradient in shallow velocities is observed (Figure 3C). The slow (<4.5 km/s) eastern portion of the peninsula correlates with the mapped location of Neogene-aged sedimentary units (V2 in Figure 3C), while the fast (>4.5 km/s) western portion of the peninsula correlates with the Torlesse Terrane (Mazengarb & Speden, 2000; V3 in Figure 3C). Additionally, the <4.5 km/s isocontours correlate with the approximate contact between these two units (Mazengarb & Speden, 2000). Lower crustal velocities of ~7 km/s are laterally homogenous above the Moho. The lithospheric mantle wedge intersects the plate interface at ~27 km depth and exhibits velocities of < 7.5 km/s beneath the Peninsula.

Offshore in the Bay of Plenty, on the western side of T1, the Australian crust thins from ~25 km in the east (transect distance 100 km) to ~20 km in the west (transect distance 25 km) due to the transition into the backarc rift of the TVZ (Figure 3C). Crustal thicknesses in the TVZ are comparable to previously calculated Moho depths from previous seismic surveys (e.g., Stratford & Stern, 2006; Gase et al., 2019). A ~3 km thick layer of slow (< 3 km/s) velocities correlate with previously observed sediment cover in the Bay of Plenty (Gase et al., 2019). The vertical velocity gradient in the mid- and lower-crust increases moving outboard from the west coast of the peninsula—from 5.5 km/s to 7 km/s in the east to 6.0 km/s to >7.0 km/s in the west.

The increase in lower-crustal velocities immediately above the Moho, from 7.0 km/s in the east to >7.0 km/s in the west, has been interpreted as an increase in fluid flux across the Moho beneath the Bay of Plenty (Gase et al., 2019). Mantle velocities beneath the Bay of Plenty are relatively laterally heterogeneous and vertically smooth, increasing from ~7.8 km/s at the Moho to ~8.5 km/s at 37 km depth, near the limit of the model ray coverage.

5.4 Gravity model

A profile was extracted from the 2-D regional free-air gravity grid of McCubbine et al. (2017) for comparison to T1 (Figure 5A). Additionally, during offshore seismic data acquisition, the *R/V Langseth* collected shipborne gravity measurements along the marine portions of T1 (Figure 5A). These two datasets provide a template to which a calculated gravity anomaly model can be compared. By converting the T1 velocities to density and comparing the resulting free air gravity anomaly to these outside datasets, geometrical constraints can be placed on the seismic velocity profile. Further constraints can be placed on the calculated velocities by comparing the converted T1 density model to sediment density measurements collected from nearby IODP boreholes (Figure 2, 3C; Barnes et al., 2019; Saffer et al., 2019).

We converted the T1 velocity structure to density using the empirically derived Nafe-Drake equation (Ludwig et al., 1970; Brocher, 2005) (Figure 5B, 5D). Because the ray coverage only provides constraints to a depth of ~50 km, simple 2-D density bodies were constructed to account for the long wavelength contributions from the subducting slab and mantle wedge (Figure S13). The top of the slab was continued downdip to a depth of 250 km following the plate interface model of Williams et al. (2013). The bottom of the slab was fixed so that the extended slab maintained a thickness of 12 km, approximating the slab thickness from the velocity results. Constant densities were applied to the extended slab and Pacific and Australian mantle. Crustal velocities for the Pacific and Australian plates were laterally extended 100 km from either end of the forward model to further accommodate long wavelength gravity anomalies and to account for poor ray coverage at the edge of the model. Densities in Bay of Plenty were reduced by 1% in the upper 1 km of the model to better fit the observed gravity signature, and densities in the Pacific were reduced by 5% in the upper 2 km of the model to better fit the gravity signature and measured IODP borehole sediment densities (Barnes et al., 2019; Saffer et al., 2019; Figure 5). Densities were increased by 2% in a polygon the approximate shape of the high velocity above the plate interface and below the inner prism (V1 in Figure 3C) to better match the observed gravity anomaly (G1 in Figure 5). A density reduction of 2% was applied to an elliptical region beneath the Bay of Plenty (G2 Figure 5) in the approximate location of previously interpreted frozen volcanic sills (Gase et al., 2019; R1 in Figure 3A). Using the converted and extended density model, the 2-D free-air gravity effect was calculated using the line integral method of Bott (1965; Figure 5A).

The SHIRE calculated free-air gravity anomaly fits the extracted McCubbine et al. (2017) profile with an RMS of 13 mGal before adjusting and 9 mGal after adjusting (Figure 5A). The two biggest sources of misfit between the calculated and observed models comes from edge

effects, due to the resolution and ray coverage limits of the tomography model near the ends of the transect, and high frequency effects of topography and bathymetry, which are difficult to capture with a smoothed velocity model. The incoming Pacific plate displays a decreasing gravity anomaly, reaching a minimum at the trench. The frontal prism produces an increase in the anomaly with shallow, low-density basins contributing to short wavelength decreases in the gravity anomaly. Onshore, a clear east-west dichotomy in the gravity signature is observed, correlating with the intersection of the Australian Moho and the plate interface imprinted on top of the lower density Neogene units in the east compared to the higher density Torlesse Terrane in the west. Gravity anomalies increase moving into the Bay of Plenty and the high gravity signature of the backarc rift (McCubbine et al., 2017).

Comparing the modified densities to the empirical Nafe-Drake equation, as well as several other rock-type specific empirical models and in situ measured density-velocity values from IODP boreholes, reveals where specific lithologies may be present. Density reductions in the Bay of Plenty and Pacific plate sediment cover agrees well with the measured density-velocity measurements from nearby IODP boreholes (Barnes et al., 2019; Saffer et al., 2019; Figure 5D). The increased density in the high velocity region above the plate interface and below the inner prism places the modelled density-velocity values closer to the Gardner empirical relation for sedimentary rocks (Gardner et al., 1974; G1 in Figure 5).

6 Discussion

6.1 Comparison to regional earthquake tomography

A New Zealand wide Vp model developed from local earthquake tomography (Eberhart-Phillips et al., 2010; Eberhart-Phillips et al., 2020) is generally compatible with the T1 Vp result (Figure 6). The prominent east-west lateral variation of shallow Australian crust velocities is apparent in both results. The Eberhart-Phillips et al. (2020) model showed slower velocities in the deeper portions of the Pacific slab compared to T1. Conversely, mid- and lower-crustal velocities in the Australian crust beneath the Raukumara Peninsula in the Eberhart-Phillips et al. (2020) model are slower than in T1; ~6.5 km/s compared to ~7.0 km/s. However, this region of the Eberhart-Phillips et al. (2020) model is characterized by sparse vertical and lateral grid spacing.

The difference between deeper slab velocities seen in Eberhart-Phillips et al. (2020) compared to T1 are a result of differing ray coverage in this region between calculations. Eberhart-Phillips et al. (2020) utilized regional events maximum hypocentral depths down to >100 km. In comparison, T1 events were limited to events with depths <~50 km due to the resolution limit of the array. As a result, Eberhart-Phillips et al. (2020) had greater ray coverage at greater depths compared to T1. However, where T1 does have ray coverage, ray densities are much greater than that of Eberhart-Phillips et al. (2020) resulting in more well constrained velocities above ~50 km depth. Additionally, shallow ray coverage of the Eberhart-Phillips et al. (2020) model is limited by the coarse instrument spacing compared to SHIRE, which also reduces the resolution of the Eberhart-Phillips et al. (2020) model in the shallow crust.

590 6.2 Forearc upper plate structure

591 Cross-sectional Neogene and ECA unit boundaries correlate well with the velocity
592 isocontours <5.0 km/s in the upper Australian crust (Mazengarb & Speden, 2000). Because the
593 Neogene and ECA units are both calcareous mudstone of similar ages (Mazengarb & Speden,
594 2000), they are expected to have similar P-wave velocities (Faust, 1951). The similar physical
595 properties of the Neogene and ECA units is further exemplified by the near surface high
596 conductivity body from Heise et al. (2017; C1 in Figure 7C). Low Qp (<250) from the Eberhart-
597 Phillips et al. (2015, 2020) attenuation calculation revealed a highly attenuative area in the
598 eastern portion of the Raukumara Peninsula, correlating with the T1 Vp region where velocities
599 are < ~5.0 km/s (Q1 in Figure 7C). These features also correlate with the velocity isocontours
600 and overall mapped structure of these units (Mazengarb & Speden, 2000). As a result, it is
601 difficult to identify a clear boundary between the Neogene and ECA units in the T1 velocity
602 result (Figure 7C).

603 Velocity-depth values measured by Christensen & Mooney (1995) can be compared to
604 calculated velocities from SHIRE to estimate where certain lithologies may be present in T1.
605 Figure 7D shows an example 1-D velocity-depth profile taken from T1 at transect distance 175
606 km. Where the calculated SHIRE Vp falls within the standard deviation of measured
607 metagraywacke (MG in Figure 7D) and greenschist (US in Figure 7D) velocities from
608 Christensen & Mooney (1995) are then shaded in Figure 7C. US in Figure 7D correlates with the
609 location of R2 in Figure 3A, suggesting that underplated sediments exhibit expected velocities
610 for greenschists (Christensen & Mooney, 1995). Velocity-depth values for metagraywacke (MG
611 in Figure 7C) reveals a good match with velocities near the surface and the mapped location of
612 the Torlesse Terrane (Mazengarb & Speden, 2000; Christensen & Okaya, 2007). We can use the
613 velocity-depth measurements of metagraywacke to extrapolate the location of the Torlesse
614 Terrane beneath the Raukumara Peninsula (MG in Figure 7C) to better understand the regional
615 basement lithology.

616 Velocities in T1 which corresponded to metagraywacke values are highlighted as feature
617 MG in Figure 7C. Given the similar velocities to the Torlesse graywacke lithology and
618 correspondence of these velocities to the shallowly mapped portions of the Torlesse Terrane, this
619 region (MG in Figure 7C) is interpreted as the extent of the Torlesse within T1. The Torlesse
620 generally maintains a consistent thickness while it dips to the east. The westernmost portion of
621 the interpreted Torlesse is relatively thinner (MG in Figure 7C) where it becomes difficult to
622 interpret the distribution of the terrane beneath the Bay of Plenty. While the Torlesse likely
623 extends into the Bay of Plenty (e.g., Leonard et al., 2010) it's extent at depth is uncertain.
624 Additionally, because thermal gradients within the Bay of Plenty are likely to modulate
625 measured velocities, we avoid interpreting velocity-depth values in this region. In the eastern
626 half of the Raukumara Peninsula, where the Torlesse abuts the plate interface, slab thickness
627 reaches a minimum of ~8 km (Figure 7A), slab dip remains constant at ~14° (Figure 7A) and a
628 noticeable change in slab coupling occurs (Figure 7B). Horizonal stress rates from GPS data
629 analyzed by Dimitrova et al. (2016) revealed that the eastern half of the Raukumara Peninsula is

generally under an extensional regime, with a patch of compression observed beneath Gisborne. Heise et al. (2017) correlated this patch of compression with a resistive body on the plate interface, which was interpreted as reduced fluid and/or sediments near the plate interface.

The combination of these observations near the Torlesse-interface intersection suggests that the Torlesse may act as a more competent, ridged backstop compared to the softer, deforming backstop observed offshore by Gase et al. (2021). This agrees with the interpreted location of the Torlesse-controlled backstop interpreted by Bassett et al. (2022). This also fits with the observations of Bland et al (2015) from the southern Hikurangi and suggests that the Torlesse plays an important role as a rigid backstop along the entire length of the Hikurangi margin and, at least in the northern Hikurangi, may be acting as a rigid backstop, promoting bending of the slab updip from this region by exerting stresses on the slab. The interpreted extent of the Torlesse backstop is also correlated with the limit of upper plate faulting as interpreted by Mountjoy & Barnes (2011), underscoring the important role the Torlesse plays in controlling regional stresses. Seismogenically, the intersection of the Torlesse with the slab does not appear to influence the occurrence of plate interface earthquakes, but this bending may reactivate pre-existing faults in the slab which then release fluids that drive SSEs (McGinty et al., 2000; Du et al., 2004; Henrys et al., 2013; Yarce et al., 2021; Mochizuki et al., 2021).

Deeper onshore 3-D resistivity models revealed a trench-parallel band of high conductivity between 25 and 30 km depth interpreted as the base of underplated sediments (C2 in Figure 7C; Heise et al., 2012; Heise et al., 2017). The conductive body interpreted by Heise et al. intersects T1 near the intersection of the Australian Moho and the plate interface and correlates with our interpreted lower crustal high reflectivity zone (R2 in Figure 3A). T1 Vp suggests this conductive body is entirely within the Australian plate crustal rocks, supporting the interpretation that this region represents a body of underplated sediments (Heise et al., 2012). Regional tomography performed by Bassett et al. (2010) also revealed lower crustal material up dip of the slab-Moho intersection. However, our high reflectivity zone and the lower crustal feature of Bassett et al. (2010) is more laterally continuous than the conductive body from Heise et al. (2012). Comparing T1 lower crustal velocities to published velocity-depth measurements for greenschist Vp (Christensen & Mooney, 1995), a ~5 km thick region correlates well with the lateral extent and estimated thickness of the reflective lower crust (Figure 3). Additionally, this region of interpreted underplated sediments correlates with the topographic high observed in the northern Axial Ranges (Figure 7), supporting the interpretation that sediments are driving uplift along the entire Axial Ranges.

6.3 Pacific slab and mantle

Reflection profiles from Bell et al. (2010) revealed a zone of high-amplitude interface reflectivity which was interpreted as a layer of volcaniclastic sediments entrained with a subducting seamount (Barker et al., 2018; Bangs et al., 2023). The seamount is located within the late 2014 Gisborne SSE but falls between two patches of large slip (> 10 cm) within the SSE (Wallace et al., 2016; Bangs et al., 2023; Figure 2), pointing to the importance of this seamount

in the distribution of effective stress as well as fluid flux within any underthrusted sediments (Bell et al., 2010). T1 passes ~20 km southwest of the interpreted seamount boundary, where Bangs et al. (2023) interpreted carbonates and consolidated turbidites from 3-D reflection data. The derived density and gravity model from T1 supports interpretation, as densities modified to fit the observed gravity anomaly (G1 in Figure 5) are aligned with expected velocities-densities for sedimentary rocks (Gardner et al., 1974).

The gap in seismicity seen by Yarce et al. (2019) near the downdip edge of the late 2014 SSE correlates with a patch of slightly elevated coupling (Wallace et al., 2012; Dimitrova et al., 2016; Heise et al., 2017; Figure 7B). Faults created by bending of the slab enable seismicity and promote fluid flux out of the slab, increasing pore pressures at the plate interface, and promoting SSEs (Yarce et al., 2019; Warren-Smith et al., 2019). Down dip of this zone of fluid release, SSE rupture stops and slab dip remains constant (Figure 7).

A cluster of intraslab seismicity at ~25 km depth (E2 in Figure 7), down dip of the Yarce et al. (2019) gap, is located near a region of constant slab dip and minimum slab thickness (Figure 7A). Above this cluster of seismicity, a region of high Vp/Vs (H1 in Figure 7C) extends from the plate interface to the surface near the east coast of the Raukumara Peninsula (Eberhart-Phillips et al., 2020). Focal mechanisms in and around this cluster show primarily normal fault mechanisms (Figure 7C) and have been observed along strike in the southern Hikurangi at similar depths (McGinty et al., 2000; Du et al., 2004; Reyners and Bannister, 2007) pointing to extensional stresses in the slab. Normal faults present in the Hikurangi Plateau (Plaza-Faverola et al., 2012) are inherited by the subducting slab (Henrys et al., 2013) and reactivated by bending stresses and/or increased fluid pressures. Temperatures of ~350°C (Antriasian et al., 2019) and approximate lithostatic pressures of ~0.8 GPa place this cluster near the metamorphic facies transition from greenschist to blueschist, where the breakdown of chlorite is expected to release ~1 wt% of water (Condit et al., 2020). The body of high Vp/Vs (H1 in Figure 7C) crosses the plate interface, suggesting a permeable plate interface at these depths, allowing fluids to migrate from the slab to the surface where they appear onshore in thermal springs (Reyes et al., 2010).

Onshore thermal springs of the Raukumara Peninsula exhibit fluids with a mantle component (Reyes et al., 2010), suggesting that the normal faults in the slab extend into the Pacific lithospheric mantle, potentially acting as conduits for fluids out of the mantle. However, the exact source of these fluids within the subduction system, as well as the pathway which they take to reach the surface, remains unclear. Resistivity (Heise et al., 2017) and regional scale Vp/Vs calculations (Eberhart-Phillips et al., 2020) indicate shallow dewatering of the slab, but this does not reconcile with the deeper isotopic signature seen in the fluids (Reyes et al., 2010). Low mantle velocities from NIGHT (Figure 1) beneath the central TVZ indicate a hydrated or partially molten mantle in the central Hikurangi, with fluids released by the serpentinization of the subducting plate (Harrison & White, 2006). However, MANGO (Figure 1) revealed little subduction-driven hydration in the northernmost Hikurangi mantle wedge (Scherwath et al., 2010).

In the Pacific mantle, immediately beneath the prism, slightly depressed velocities (~7.5 km/s) are observed, previously interpreted as serpentinized mantle (Grevemeyer et al., 2018; Gase et al., 2021; Bassett et al., 2022). As serpentinization requires temperatures <~400°C (Bach et al., 2004), this is consistent with observed upper mantle temperatures of 200-600°C from 2-D thermal models of the northern Hikurangi (Antriasian et al., 2019). Events recorded by the GeoNet national seismic catalog from 2009-2019 (www.geonet.org.nz) within +/- 10 km of T1 reveal a cluster of seismicity immediately below this low velocity area at a depth of ~25 km within a zone of low (<1.65) Vp/Vs ratios (Eberhart-Phillips et al., 2020; L1 and E1 Figure 7C), potentially indicating a zone of dehydration embrittlement in the mantle. Moment tensors calculated by GeoNet from 2003 to present (www.github.com/GeoNet) reveals primarily normal faulting mechanisms surrounding this cluster. Such mechanisms are expected for dehydration reactions, where volumetric changes lead to normal faulting (Green & Houston, 1995). Additionally, throughgoing faults are thought to hydraulically connect the mantle with the Pacific slab in the Hikurangi, promoting the flux of fluid from the mantle, through the slab, and perhaps into the overriding plate (e.g., Reyes et al., 2010; Henrys et al., 2013). However, serpentinized mantle is expected to have high (>1.9) Vp/Vs ratios (e.g., Grevemeyer et al., 2018), which is absent from this area. If there are fluids in the upper mantle, they are removed from the region before serpentinization can occur, leading to a dry, brittle mantle promoting clustered seismicity (E1 in Figure 7C). Alternatively, or in addition to serpentinization, fractures in the upper mantle can also lead to lower Vp (e.g., Mark et al., 2023; Miller et al., 2021). This interpretation is also consistent with the observation of seismicity in this region, and would also have implications for upper mantle anisotropy (Mark et al., 2023).

6.4 Comparison to previous seismic transects

6.4.1 SAHKE

SAHKE velocities in the incoming plate, slab, and overriding plate (Henrys et al., 2013; Figures 8A, 8B) are comparable to those calculated from T1 (Figures 8A, 8C). Like SHIRE, SAHKE also exhibited a cluster of intraslab seismicity associated with an increase in slab dip (Henrys et al., 2013). However, updip from this zone, the slab in the SAHKE model dips < 5° (Henrys et al., 2013), whereas the slab in the SHIRE profile dips > 5° (Figure 8). The plate interface imaged in SAHKE has a noticeable increase in slab dip ~127 km inboard from the trench at a depth of ~25 km. The difference in slab dip between north and south implies along strike variations in the backstop and/or slab bending stresses, with additional stress exerted on the slab in the northern Hikurangi causing a larger slab dip in this region. A zone of low seismic velocities and high reflectivity is also observed in SAHKE near the intersection of the Australian Moho and plate interface and near the transition from locked to creeping plate interface behavior. However, this region is both seismically slower (~6.0-7.0 km/s) and laterally narrower than the zone observed in SHIRE. This pocket of reflectivity in SAHKE is bounded by a ramp thrust fault and the Wairarapa Fault and is located immediately updip of the Moho-interface intersection (Henrys et al., 2013), as opposed to immediately above the Moho as in SHIRE. This suggests

749 that the underplated duplexes of sediment interpreted in SAHKE do not interact with the
750 Australian mantle nose. Furthermore, the underplated sediments in the southern Hikurangi are
751 most likely Mesozoic turbidites from the Chatham Rise that have been shown to more readily
752 subduct compared to sediments in the north (Crutchley et al., 2020; Gase et al., 2022).
753
754 6.4.2 NIGHT
755 Wide-angle OBS, near-vertical onshore, and MCS data revealed a subduction interface at
756 ~18-20 km beneath Hawke Bay, with a 10-12 km thick Hikurangi Plateau comprising the
757 subducting oceanic crust (Pecher et al., 2002; Henrys et al., 2003; Figure 8). Because of the high
758 rate of lower crustal magmatism and heat flux as described in Henrys et al. (2003), there is a
759 more gradational transition between the crust and the mantle, resulting in little to no *PmP* energy
760 appearing in the wide-angle data. The crustal thickness in the TVZ of the central Hikurangi is
761 ~25 km (Stern & Benson, 2011), comparable to the surrounding regional thickness of 20-28 km
762 (Henrys et al., 2003; Stratford & Stern, 2006). Similar to SAHKE, the NIGHT transect revealed
763 a shallow (> 5°) slab dip near the trench, with a marked increase in slab dip near a cluster of
764 seismicity below the plate interface ~126 km inboard from the trench at a depth of ~15 km
765 (Henrys et al., 2003).
766 A conductive anomaly between 20 and 35 km depth is present away from the top of the
767 slab beneath the onshore portion of the NIGHT transect (Ogawa et al., 1999; Henrys et al.,
768 2003), similar to the placement of the conductive body seen near the SHIRE transect, which has
769 been interpreted to be underplated sediments (Heise et al., 2012; 2017). However, this
770 conductive anomaly was associated with a highly reflective boundary by Stern & Benson (2011),
771 where it was interpreted as a body of pooled melt stalled near the eastern edge of the TVZ. Given
772 that this region is ~100 km northwest of the Axial Ranges, it seems unlikely this is evidence for
773 underplated sediments. Slow (6.0-6.5 km/s) lower crustal velocities beneath the Axial Ranges
774 may indicate the presence of underplated sediments near the intersection of the plate interface
775 and the Australian Moho, although this would need to be confirmed by additional geophysical
776 imaging and interpretation. However, this potential along strike transition of underplated
777 sediment location suggests and along strike control on the kinematics driving underplating.
778
779 6.4.3 MANGO
780 Tomographic Vp models from the MANGO experiment (Figure 8) reveals a plate
781 interface geometry more similar to SHIRE than to SAHKE or NIGHT (Henrys et al., 2013;
782 Henrys et al., 2003; Bassett et al., 2016). The slab in MANGO dips ~8° near the trench,
783 comparable to the SHIRE dip of ~7° and greater than the <5° dip seen in SAHKE and NIGHT
784 (Henrys et al., 2013; Henrys et al., 2003; Bassett et al., 2016). At a depth of ~19 km, the slab dip
785 increases to 18° (Bassett et al., 2016) and correlates with an increase in seismicity
786 (www.geonet.org.nz). This margin-wide relation between slab dip and seismicity, with an updip
787 shift in shallow slab dip moving south to north along the Hikurangi, suggests a broader influence
788 of the upper plate on the structure of the subducting slab. Results from MANGO also revealed

low velocities immediately downdip of the transition from a locked to creeping interface, suggesting that underplated sediment may run the entire length of the Hikurangi Margin, including offshore (Bassett et al., 2010; Henrys et al., 2013; Bassett et al., 2016). While the entrainment of sediments near the down-dip frictional transition in plate interface behavior is similar to SAHKE, it is dissimilar to the underplated sediment location from SHIRE and, ostensibly, NIGHT. Furthermore, unlike SAHKE, NIGHT, and SHIRE, the underplated sediment appear updip of the notable increase in slab bend.

6.4.4 Along-strike comparisons

An increase in slab dip at a depth of ~20-30 km is observed along the entire length of the Hikurangi margin (Figure 8). The distance between the trench and where this slab bend (from <10° to >15°) occurs decreases from south to north, as the overall slab gradient increases along strike (Williams et al., 2013; Figure 8A). In SAHKE, the increase in slab dip was slightly downdip of a dense region of intracrustal normal faults and near the downdip extent of plate locking (Wallace et al., 2006), where the bending was interpreted as a result of the incipient weakness in the slab (Henrys et al., 2013). While incipient weakness may be the case in the south, there appears to be no correlation with the downdip extent of locking in the SHIRE profile (Figure 8). Additionally, the slab bend in the south occurs beneath the region of underplated sediment (Henrys et al., 2013; Figure 8C), whereas the SHIRE profile reveals this bending occurs up dip from the underplated sediments (Figure 8B). Furthermore, MANGO shows bending occurring downdip from underplated sediments, suggesting that the two observations are unrelated. It is possible that the slab bending is the result of increased density of the slab from greenschist to blueschist facies transformation (e.g., Condit et al., 2020) that happens to occur where preexisting faults are already present in the slab (Plaza-Faverola et al., 2012; Henrys et al., 2013; Figure 8).

Additionally, slab rollback is observed immediately north of the northern Hikurangi in the Havre Trough (Caratori Tontini et al., 2019). If this rollback continues into the Hikurangi, which would generally be consistent with how the arc has migrated southward (Bassett et al., 2016; Caratori Tontini et al., 2019), then this would contribute to extension and slab dip steepening in the northern Hikurangi. The trenchward shift of the slab inflection is correlated with the appearance of the TVZ (Figure 8B), suggesting that the stress regime imposed on the slab by the extensional backarc could also influence the slab dip on a regional scale with upper plate and/or slab properties controlling slab dip on a more local scale. The increased compressional stresses experienced by the forearc in these northern profiles appears to correlate with increased bending stresses applied on the slab, suggesting rift-related stress may be transferred through the forearc.

While underplated sediments correlate with the downdip extent of plate interface locking in the SAHKE and MANGO profiles, no such correlation is observed in the NIGHT and SHIRE profiles (Figure 8). This suggests that factors such as subducting sediment composition and/or the upper-plate stress state control the depth to locking along the Hikurangi. The southern

Hikurangi are largely thick turbidites, whereas volcaniclastic sediments and an extensional backarc characterize the north (Gase et al., 2022). The presence of the Torlesse Terrane near the downdip extent of locking on the plate interface suggests this may be an influencing factor in the north, no such correlation exists in the south (Bassett et al., 2022) suggesting that the Torlesse may have some impact on shallow frictional transitions but not deeper transitions.

With the observation of underplated sediment along the T1 profile, sediments are revealed via tomography to be present in the southern (SAHKE; Henrys et al., 2013), central (NIGHT; Henrys et al., 2003), northern (this study), and offshore (MANGO; Scherwath et al., 2010) segments of the Hikurangi Margin. The location of underplated sediments along the entire length of the Hikurangi correlates well with topographic highs (Figure 8) supporting the interpretation that underplating is driving uplift of the Axial Ranges (Sutherland et al., 2009; Scherwath et al., 2010). As the low-density subducted sediment reaches the high-density cold mantle nose, the density contrast forces the sediments to accrete to the bottom of the Australian plate, creating buoyancy that lifts the Axial Ranges. Furthermore, the narrow width of the underplated sediment package in the south (Henrys et al., 2013) correlates with the relatively narrow width of the southern Axial Ranges. As the width of the sediment increases, the width of the Axial Ranges also increases, particularly in the forearc adjacent to the TVZ (Figure 8). While there appears to be a geometrical correlation between underplated sediment and locked-to-creeping plate interface transition in the SAHKE and MANGO profiles, SHIRE and NIGHT do not show such a correlation. Evidence from SHIRE points to a stronger influence from the upper plate structure on the interface behavior. However, understanding the the relationship of the Torlesse Terrane to down-dip geodectic plate coupling transitions in the southern Hikurangi requires additional work.

The change in slab bending stresses may also influence the geometry of the underplated sediments observed along the margin. Henrys et al. (2006) interpret a laterally narrow packet of underplated sediments between the slab and the upper plate. However, the interpreted underplated sediments from the SHIRE profile are both laterally wider and deeper than the SAHKE observations—evidence from SHIRE suggests the sediments are underplating the Australian crust immediately above the cold lithospheric mantle nose. The extensional stresses of the TVZ, a step down in the megathrust (e.g., Henrys et al., 2013), seamount collision (Bangs et al., 2006), and/or the observed extension beneath the Raukumara Peninsula (Dimitrova et al., 2016) could create the space needed for sediments to be laterally underplated. This would explain the characteristic change in lower crustal reflectivity between SAHKE and SHIRE, as well as the resulting increase in Axial Range width, from ~30 km in the south to ~75 km in the north along the Hikurangi. Both the increased Axial Range width and the shallower slab bending in the northern Hikurangi could be a result of the additional compressional stresses experienced by the forearc from the TVZ backarc.

The northern Hikurangi margin is more (pelagic and hemipelagic) sediment starved relative to the south (Fagereng, 2011; Wang et al., 2010). However, the north appears to have a wider zone and larger volume of underplated sediments (Figure 8). Rather than entrained marine

sediments brought down from the surface in a subduction channel, these sediments may come from the upper plate, as the northern Hikurangi may exhibit a higher degree of tectonic erosion relative to the south (Fagereng, 2011; Wang et al., 2010). While the northern Hikurangi does not display the tectonic erosion signature of trenchward advection of the forearc (Bassett et al., 2020), cyclical underplating kinematics proposed by Sutherland et al. (2009) and Bassett et al. (2010) would explain the lack of advection in the northern Hikurangi. The source of sediments would have ramifications for the composition of the underplating along the entire Hikurangi Margin. However, the effects of locking and varying degree of subduction interface gradient between the northern and southern Hikurangi may either influence or be influenced by the sediment budget in the margin. Gase et al. (2022) identified a thinner sediment subduction channel in the creeping section of the Hikurangi immediately north of the transition from the locked southern Hikurangi. This would suggest that underplated material in the south are comprised of a higher degree of down going pelagic and siliciclastic sediments. However, the higher degree of coupling (Wallace et al., 2004) and shallower slab gradient in the south (Figure 8) may result in a higher rate of subduction erosion. Localized regions of plate locking in the north (Dimitrova et al., 2016) and/or seamounts may provide sources of sediments, particularly volcaniclastic sediments (Gase et al., 2021; 2022) or the upper crust of the Hikurangi Plateau (e.g., Timm et al., 2014).

Numerical modelling from Litchfield et al. (2007) predicts a broad region of uplift in the northern Hikurangi margin associated with underplated sediment. However, their modelling was performed prior to the crustal constraints of SAHKE, NIGHT, MANGO, and SHIRE, and included a relatively narrow package of underplated sediments, not the more laterally continuous sediments accreted to the lower Australian crust as interpreted here. This, combined with the lack of underplated sediment modelling in the southern Hikurangi by Litchfield et al. (2007), suggests that additional geodynamical modelling using the well constrained crustal structure from this study and Henrys et al. (2013) is needed. This could help reveal the connection between underplated sediment geometry and Axial Range width and can include the effects of the TVZ to better understand the role backarc extension has on underplated sediment accretion and forearc uplift.

7 Conclusions

1. SHIRE Transect 1 characterizes the breadth of the northern Hikurangi subduction system, revealing structure and properties of the incoming Pacific plate, trench, accretionary prism, downgoing slab, overlying Australian plate and backarc TVZ rift.
2. The east to west transition of shallow velocities in the Raukumara Peninsula is correlated with Neogene and Cretaceous aged sedimentary units. This allows for the vertical extrapolation of units at depth, based on existing lab measured velocity-depth values for relevant lithologies, to determine basement lithologies.

3. The location of the Cretaceous-aged Torlesse Terrain at depth and its interpreted influence on subducting slab properties suggests it plays a role as a rigid backstop behind the more actively deforming frontal wedge in the northern Hikurangi.
4. Dehydration embrittlement in the Pacific mantle beneath the accretionary wedge may be releasing fluids which are transported through the subducting slab via conductive normal faults and across a permeable plate interface.
5. An increase in slab dip is observed at ~20-30 km depth along the length of the Hikurangi margin, representing metamorphic phase transitions and/or bending stresses applied by the upperplate forearc.
6. Sediment underplating beneath the Australian crust, with sediments possibly sourced from the upper plate, is driving uplift of the entire North Island Axial Ranges and the width of the underplated sediment package controls the width of the uplifted topography.

Acknowledgements

This study was funded by US NSF FRES program EAR-1616847 (TWL, DAO), EAR-161581 (ACG, HVA, NLB); NZ participation is supported by the New Zealand Ministry of Business, Innovation and Employment (MBIE) Endeavour Grant: Diagnosing peril posed by the Hikurangi subduction zone, and by public research funding from MBIE Strategic Science Investment Fund to GNS Science. We thank Wiebke Heise for providing the resistivity data; Robert Harris for providing the Hikurangi thermal data; and Cailey Condit, Kyle Bland, and Dominic Strogen for their insightful discussions. We also thank Lloyd Carothers, Alissa Scire, the landowners for hosting seismic sites, and the entire SHIRE field team for their efforts in collecting the onshore data. We are grateful to individual landowners and companies who enabled the data collection by hosting seismograph sites on their properties. We would also like to thank the Tairāwhiti/Raukumara communities for engaging with us, particularly Māori iwi involved in the SHIRE project. Finally, we acknowledge the following organisations for providing resource consents: Bay of Plenty Regional Council, Gisborne District Council, Hawke's Bay Regional Council, Ōpōtiki District Council, and Heritage New Zealand Pouhere Taonga.

,.

References

Antriasian, A., Harris, R. N., Tr, A. M., Henrys, S. A., Phrampus, J., Lauer, R., Gorman, A. R., Pecher, I. A., & Barker, D. (2019). *Thermal regime of the Northern Hikurangi margin, New Zealand*. 1177–1190. https://doi.org/10.1093/gji/ggy450

Arnulf, A. F., Biemiller, J., Lavier, L., Wallace, L. M., Bassett, D., Henrys, S., Pecher, I., Crutchley, G., & Plaza Faverola, A. (2021). Physical conditions and frictional properties in the source region of a slow-slip event. *Nature Geoscience*, *14*(5), 334–340. https://doi.org/10.1038/s41561-021-00741-0

Ballance, P. F. (1976). Evolution of the Upper Cenozoic magmatic arc and plate boundary in northern New Zealand. Earth and Planetary Science Letters, 28(3), 356–370. https://doi.org/10.1016/0012-821x(76)90197-7

949 Bangs N, Ship Board Science Party. 2018. SHIRE Project Cruise Report: Seismogenesis at
950 Hikurangi Integrated Research Experiment, November 1 - December 7, 2017. Austin
951 (TX): University of Texas Institute of Geophysics.
952 Barker, D. H. N., R. Sutherland, S. Henrys, and S. Bannister (2009), Geometry of the Hikurangi
953 subduction thrust and upperplate, North Island, New Zealand,Geochem. Geophys.
954 Geosyst.,10, Q02007, doi:10.1029/2008GC002153.
955 Barker, D. H. N., Henrys, S., Caratori Tontini, F., Barnes, P. M., Bassett, D., Todd, E., &
956 Wallace, L. (2018). Geophysical Constraints on the Relationship Between Seamount
957 Subduction, Slow Slip, and Tremor at the North Hikurangi Subduction Zone, New
958 Zealand. *Geophysical Research Letters*, *45*(23), 12,804-12,813.
959 https://doi.org/10.1029/2018GL080259
960 Barker, D. H. N., Van Avendonk, H., & Fujie, G. (2019). Seismogenesis at Hikurangi Integrated
961 Research Experiment (SHIRE) report of RV Tangaroa cruise TAN1710, 23 Oct-20 Nov
962 2017 (GNS Science report 2019/01). GNS Science. https://doi.org/10.21420/H28Y-5N43
963 Barnes, P. M., Lamarche, G., Bialas, J., Henrys, S., Pecher, I., Netzeband, G. L., Greinert, J.,
964 Mountjoy, J. J., Pedley, K., & Crutchley, G. (2010). Tectonic and geological framework
965 for gas hydrates and cold seeps on the Hikurangi subduction margin, New Zealand.
966 *Marine Geology*, *272*(1–4), 26–48. https://doi.org/10.1016/j.margeo.2009.03.012
967 Barnes, P. M., Pecher, I. A., Levay, L. J., Bourlange, S. M., Brunet, M. M. Y., Cardona, S.,
968 Woodhouse, A. D., & Wu, H. (2019). *Expedition 372A summary*. *372*(May).
969 Barnes, P. M., Wallace, L. M., Saffer, D. M., Bell, R. E., Underwood, M. B., Fagereng, A.,
970 Meneghini, F., Savage, H. M., Rabinowitz, H. S., Morgan, J. K., Kitajima, H., Kutterolf,
971 S., Hashimoto, Y., Engelmann De Oliveira, C. H., Noda, A., Crundwell, M. P., Shepherd,
972 C. L., Woodhouse, A. D., Harris, R. N., … LeVay, L. J. (2020). Slow slip source
973 characterized by lithological and geometric heterogeneity. *Science Advances*, *6*(13), 1–
974 11. https://doi.org/10.1126/sciadv.aay3314
975 Bassett, D., Arnulf, A., Henrys, S., Barker, D., van Avendonk, H., Bangs, N., Kodaira, S.,
976 Seebeck, H., Wallace, L., Gase, A., Luckie, T., Jacobs, K., Tozer, B., Arai, R., Okaya, D.,
977 Mochizuki, K., Fujie, G., & Yamamoto, Y. (2022). Crustal Structure of the Hikurangi
978 Margin From SHIRE Seismic Data and the Relationship Between Forearc Structure and
979 Shallow Megathrust Slip Behavior. *Geophysical Research Letters*, *49*(2), 1–11.
980 https://doi.org/10.1029/2021GL096960
981 Bassett, D., Kopp, H., Sutherland, R., Henrys, S., Watts, A. B., Timm, C., Scherwath, M.,
982 Grevemeyer, I., & Ronde, C. E. J. (2016). Crustal structure of the Kermadec arc from
983 MANGO seismic refraction profiles. *Journal of Geophysical Research: Solid Earth*,
984 *121*(10), 7514–7546. https://doi.org/10.1002/2016JB013194
985 Bell, R., Sutherland, R., Barker, D. H. N., Henrys, S., Bannister, S., Wallace, L., & Beavan, J.
986 (2010). Seismic reflection character of the Hikurangi subduction interface, New Zealand,
987 in the region of repeated Gisborne slow slip events. *Geophysical Journal International*,
988 *180*(1), 34–48. https://doi.org/10.1111/j.1365-246X.2009.04401.x
989 Bland, K. J., Uruski, C. I., & Isaac, M. J. (2015). Pegasus Basin, eastern New Zealand: A
990 stratigraphic record of subsidence and subduction, ancient and modern. New Zealand
991 Journal of Geology and Geophysics, 58(4), 319–343.
992 https://doi.org/10.1080/00288306.2015.1076862

993 Bott, M. (1965), The deep sructure of the Northern Irish Sea-a problem of crustal dynamics, in
994 Submarine Geology and Geophysics, edited by W. F. Whittard and R. Bradshaw, Colston
995 Pap., vol. 17, pp. 179–204 Butterworth, London.
996 Brocher, T. M. (2005). Empirical relations between elastic wave speeds and density in the
997 Earth's crust. Bulletin of the Seismological Society of America, 95(6), 2081–2092.
998 https://doi.org/10.1785/0120050077
999 Brothers, R. N. (1984). Subduction regression and oceanward migration of volcanism, North
1000 Island, New Zealand. Nature, 309(5970), 698. https://doi.org/10.1038/309698a0
1001 Caratori Tontini, F., Bassett, D., de Ronde, C. E., Timm, C., & Wysoczanski, R. (2019). Early
1002 evolution of a young back-arc basin in the Havre Trough. Nature Geoscience, 12(10),
1003 856-862.
1004 Chesley, C., Naif, S., Key, K., & Bassett, D. (2021). Fluid-rich subducting topography generates
1005 anomalous forearc porosity. Nature, 595(7866), 255–260. https://doi.org/10.1038/s41586-
1006 021-03619-8
1007 Christensen, N. I., & Mooney, W. D. (1995). Seismic velocity structure and composition of the
1008 continental crust: A global view. Journal of Geophysical Research, 100(B6), 9761–9788.
1009 https://doi.org/10.1029/95JB00259
1010 Christensen, N. I., & Okaya, D. A. (2007). Compressional and shear wave velocities in south
1011 island, New Zealand rocks and their application to the interpretation of seismological
1012 models of the New Zealand crust. Geophysical Monograph Series, 175, 123–155.
1013 https://doi.org/10.1029/175GM08
1014 Clark, R. H., Cole, J. W. (1986). White Island. In: Smith, I. E. M. ed. Late Cenozoic volcanism
1015 in New Zealand. Royal Society of New Zealand bulletin 23:169-178.
1016 Cole, J. W., Thordarson, T., & Burt, R. M. (2000). Magma origin and evolution of white Island
1017 (Whakaari) volcano, Bay of Plenty, New Zealand. *Journal of Petrology*, *41*(6), 867–895.
1018 https://doi.org/10.1093/petrology/41.6.867
1019 Condit, C. B., Guevara, V. E., Delph, J. R., & French, M. E. (2020). Slab dehydration in warm
1020 subduction zones at depths of episodic slip and tremor. *Earth and Planetary Science*
1021 *Letters*, *552*, 116601. https://doi.org/10.1016/j.epsl.2020.116601
1022 Crampton, J. S., Mortimer, N., Bland, K. J., Strogen, D. P., Sagar, M., Hines, B. R., King, P. R.,
1023 & Seebeck, H. (2019). Cretaceous termination of subduction at the Zealandia margin of
1024 Gondwana: The view from the paleo-trench. *Gondwana Research*, *70*, 222–242.
1025 https://doi.org/10.1016/j.gr.2019.01.010
1026 Davey, F. J., Henrys, S. A., & Lodolo, E. (1995). Asymmetric rifting in a continental back-arc
1027 environment, North Island, New Zealand. Journal of Volcanology and Geothermal
1028 Research, 68, 209–238. https://doi.org/10.1016/0377-0273(95)00014-L
1029 Davy, B., Hoernle, K., & Werner, R. (2008). Hikurangi Plateau: Crustal structure, rifted
1030 formation, and Gondwana subduction history. *Geochemistry, Geophysics, Geosystems*,
1031 *9*(7). https://doi.org/10.1029/2007GC001855
1032 Dimitrova, L. L., Wallace, L. M., Haines, A. J., & Williams, C. A. (2016). High-resolution view
1033 of active tectonic deformation along the Hikurangi subduction margin and the Taupo
1034 Volcanic Zone, New Zealand. *New Zealand Journal of Geology and Geophysics*, *59*(1),
1035 43–57. https://doi.org/10.1080/00288306.2015.1127823
1036 Doser, D. I., & Webb, T. H. (2003). Source parameters of large historical (1917-1961)
1037 earthquakes, North Island, New Zealand. Geophysical Journal International, 152(3), 795–
1038 832. https://doi.org/10.1046/j.1365-246X.2003.01895.x

1039 Du, W. X., C. H. Thurber, M. E. Reyners, D. Eberhart-Phillips, and H. Zhang (2004), New
1040 constraints on seismicity in the Wellington region of New Zealand from relocated
1041 earthquake hypocentres, Geophys. J. Int., 158(3), 1088–1102.
1042 Eberhart-Phillips, D., Reyners, M., Bannister, S., Chadwick, M., & Ellis, S. (2010). Establishing
1043 a Versatile 3-D Seismic Velocity Model for New Zealand. *Seismological Research*
1044 *Letters*, *81*(6), 992–1000. https://doi.org/10.1785/gssrl.81.6.992
1045 Eberhart-Phillips, D., M. Reyners, and S. Bannister (2015), A 3-D Qp attenuation model for all
1046 of New Zealand, Seis. Res. Lett., 86, 1655-1663, doi:10.1785/0220150124.
1047 Eberhart-Phillips, Donna, Bannister, Stephen, Reyners, Martin, & Henrys, Stuart. (2020). New
1048 Zealand Wide model 2.2 seismic velocity and Qs and Qp models for New Zealand [Data
1049 set]. Zenodo. http://doi.org/10.5281/zenodo.3779523
1050 Fagereng, Å. (2011). Geology of the seismogenic subduction thrust interface. *Geological Society*
1051 *Special Publication*, *359*(1), 55–76. https://doi.org/10.1144/SP359.4
1052 Faust, L. Y. (1951). Seismic velocity as a function of depth and geologic time. Geophysics,
1053 16(2), 192.
1054 Flueh, E. R., and H. Kopp (2007), FS Sonne Fahrtbericht/cruise report SO192 MANGO: Marine
1055 geoscientific investigations on the input and output of the Kermadec subduction zone,
1056 Rep. 11, 127 pp., IFM-GEOMAR, Kiel, Germany.
1057 Gardner, G. H. F., L. W. Gardner, and A.R. Gregory (1974), Formation velocity and density –
1058 Diagnostic basics for stratigraphy traps, Geophysics, 39, 770-780.
1059 Gase, A. C., Bangs, N. L., Van Avendonk, H. J. A., Bassett, D., & Henrys, S. A. (2022).
1060 Hikurangi megathrust slip behavior influenced by lateral variability in sediment
1061 subduction. *Geology*, *July*. https://doi.org/10.1130/g50261.1
1062 Gase, A. C., Van Avendonk, H. J. A., Bangs, N. L., Bassett, D., Henrys, S. A., Barker, D. H. N.,
1063 Kodaira, S., Jacobs, K. M., Luckie, T. W., Okaya, D. A., Fujie, G., Yamamoto, Y.,
1064 Arnulf, A. F., & Arai, R. (2021). Crustal Structure of the Northern Hikurangi Margin,
1065 New Zealand: Variable Accretion and Overthrusting Plate Strength Influenced by Rough
1066 Subduction. *Journal of Geophysical Research: Solid Earth*, *126*(5), 1–26.
1067 https://doi.org/10.1029/2020JB021176
1068 Gase, A. C., Van Avendonk, H. J. A., Bangs, N. L., Luckie, T. W., Barker, D. H. N., Henrys, S.
1069 A., Bassett, D., Okaya, D. A., Jacobs, K. M., Kodaira, S., Fujie, G., Arnulf, A. F., &
1070 Yamamoto, Y. (2019). Seismic Evidence of Magmatic Rifting in the Offshore Taupo
1071 Volcanic Zone, New Zealand. *Geophysical Research Letters*, 949–957.
1072 https://doi.org/10.1029/2019GL085269
1073 Grevemeyer, I., Ranero, C. R., & Ivandic, M. (2018). Structure of oceanic crust and
1074 serpentinization at subduction trenches. Geosphere, 14(2), 1–24.
1075 https://doi.org/10.1130/ges01537.1
1076 Green, H. W., & Houston, H. (1995). The Mechanics of Deep Earthquakes. Annual Review of
1077 Earth and Planetary Sciences, 23(1), 169–213.
1078 https://doi.org/10.1146/annurev.ea.23.050195.001125
1079 Hamel, J. E., Miller, C. N., Marshall, J. S., McKinney, E., White, C. J., Zohbe, N. M., &
1080 Litchfield, N. J. (2019, December). Marine Terrace Evidence for Two Paleo-Earthquake
1081 Uplift Events Along the Southern Hawkes Bay Coastline, North Island, New Zealand.
1082 In AGU Fall Meeting Abstracts (Vol. 2019, pp. T51H-0393).

1083 Hamling, I. J., Hreinsdttir, S., Bannister, S., & Palmer, N. (2016). Odd-axis magmatism along a
1084 subaerial back-arc rift: Observations from the Taupo Volcanic Zone, New Zealand.
1085 Science Advances, 2(6), e1600288. https://doi.org/10.1126/sciadv.1600288
1086 Harrison, A., & White, R. S. (2006). Lithospheric structure of an active backarc basin: The
1087 Taupo Volcanic Zone, New Zealand. Geophysical Journal International, 167(2), 968–
1088 990. https://doi.org/10.1111/j.1365-246X.2006.03166.x
1089 Hayes, G. P., D. J. Wald, and R. L. Johnson (2012), Slab1.0: A three-dimensional model of
1090 global subduction zone geometries, J. Geophys. Res.,117, B01302,
1091 doi:10.1029/2011JB008524
1092 Heise, W., Caldwell, T. G., Bannister, S., Bertrand, E. A., Ogawa, Y., Bennie, S. L., & Ichihara,
1093 H. (2017). Mapping subduction interface coupling using magnetotellurics: Hikurangi
1094 margin, New Zealand. *Geophysical Research Letters*, *44*(18), 9261–9266.
1095 https://doi.org/10.1002/2017GL074641
1096 Heise, W., Caldwell, T. G., Hill, G. J., Bennie, S. L., Wallin, E., & Bertrand, E. A. (2012).
1097 Magnetotelluric imaging of fluid processes at the subduction interface of the Hikurangi
1098 margin, New Zealand. *Geophysical Research Letters*, *39*(4), 1–5.
1099 https://doi.org/10.1029/2011GL050150
1100 Henrys, S., Reyners, M., & Bibby, H. (2003). Exploring the Plate Boundary Structure of the
1101 North Island, New Zealand. Eos, 84(31), 294–295.
1102 Henrys, S., Reyners, M., Pecher, I., Bannister, S., Nishimura, Y., & Maslen, G. (2006). Kinking
1103 of the subducting slab by escalator normal faulting beneath the North Island of New
1104 Zealand. Geology, 34(9), 777–780. https://doi.org/10.1130/G22594.1
1105 Henrys, S., Wech, A., Sutherland, R., Stern, T., Savage, M., Sato, H., Mochizuki, K., Iwasaki,
1106 T., Okaya, D., Seward, A., Tozer, B., Townend, J., Kurashimo, E., Iidaka, T., &
1107 Ishiyama, T. (2013). SAHKE geophysical transect reveals crustal and subduction zone
1108 structure at the southern Hikurangi margin, New Zealand. *Geochemistry, Geophysics,*
1109 *Geosystems*, *14*(7), 2063–2083. https://doi.org/10.1002/ggge.20136
1110 Hoernle, K., Hauff, F., van den Bogaard, P., Werner, R., Mortimer, N., Geldmacher, J., Garbe-
1111 Schönberg, D., & Davy, B. (2010). Age and geochemistry of volcanic rocks from the
1112 Hikurangi and Manihiki oceanic Plateaus. Geochimica et Cosmochimica Acta, 74(24),
1113 7196–7219. https://doi.org/10.1016/j.gca.2010.09.030
1114 Jacobs K, Henrys SA, Okaya D, Van Avendonk H, Black J, Barker DHN, Karalliyadda SC,
1115 Kurashimo E, Stratford WR, Savage M, Sullivan R, Bruce ZR, Hughes L, SHIRE Team.
1116 2020. Seismogenesis Hikurangi Integrated Research Experiment (SHIRE): onshore
1117 seismic acquisition field report. Lower Hutt (NZ): GNS Science. 136 p. (GNS Science
1118 report; 2019/19)
1119 Kelemen, P. B., Shimizu, N., & Salters, V. J. (1995). Extraction of mid-ocean-ridge basalt from
1120 the upwelling mantle by focused flow of melt in dunite channels. Nature, 375(6534), 747-
1121 753.
1122 Kilgour, G., Kennedy, B., Scott, B., Christenson, B., Jolly, A., Asher, C., Rosenberg, M., &
1123 Saunders, K. (2021). Whakaari/White Island: A review of New Zealand's most active
1124 volcano. New Zealand Journal of Geology and Geophysics, 64(2–3), 273–295.
1125 https://doi.org/10.1080/00288306.2021.1918186
1126 Kroenke, L. W., Wessel, P., & Sterling, A. (2004). Motion of the Ontong Java Plateau in the hot-
1127 spot frame of reference: 122 Ma-present. Geological Society, London, Special
1128 Publications, 229(1), 9-20.

1129 Lamarche, G., Barnes, P. M., & Bull, J. M. (2006). Faulting and extension rate over the last
1130 20,000 years in the offshore Whakatane Graben, New Zealand continental shelf.
1131 *Tectonics*, *25*(4), 0–24. https://doi.org/10.1029/2005TC001886
1132 Lamb, S., & Smith, E. (2013). The nature of the plate interface and driving force of interseismic
1133 deformation in the New Zealand plate-boundary zone, revealed by the continuous GPS
1134 velocity field. Journal of Geophysical Research: Solid Earth, 118(6), 3160–3189.
1135 https://doi.org/10.1002/jgrb.50221
1136 Leah, H., Fagereng, Å., Bastow, I., Bell, R., Lane, V., Henrys, S., Jacobs, K., & Fry, B. (2022).
1137 The northern Hikurangi margin three-dimensional plate interface in New Zealand
1138 remains rough 100 km from the trench. Geology, XX(Xx), 1–5.
1139 https://doi.org/10.1130/g50272.1
1140 Leonard, G.S.; Begg, J.G.; Wilson, C.J.N. (compilers) 2010: Geology of the Rotorua area.
1141 Institute of Geological
1142 & Nuclear Sciences 1:250 000 geological map 5. 1 sheet + 102 p. Lower Hutt, New Zealand.
1143 GNS Science.
1144 Litchfield, N., Ellis, S., Berryman, K., & Nicol, A. (2007). Insights into subduction-related uplift
1145 along the Hikurangi Margin, New Zealand, using numerical modeling. Journal of
1146 Geophysical Research: Earth Surface, 112(2), 1–17.
1147 https://doi.org/10.1029/2006JF000535
1148 Ludwig, W. J., J. E. Nafe, and C. L. Drake (1970). Seismic refraction, in The Sea, A. E. Maxwell
1149 (Editor), Vol. 4, Wiley-Interscience, New York, 53–84.
1150 Mazengarb, C., and I. G. Speden (2000), Geology of the Raukumara area, geological map, 60
1151 pp., scale 1:250,000, GNS Sci., Lower Hutt, New Zealand.
1152 McCubbine, J. C., Stagpoole, V., Caratori Tontini, F., Amos, M., Smith, E., & Winefield, R.
1153 (2017). Gravity anomaly grids for the New Zealand region. New Zealand Journal of
1154 Geology and Geophysics, 60(4), 381–391.
1155 https://doi.org/10.1080/00288306.2017.1346692
1156 McGinty, P., Reyners, M., & Robinson, R. (2000). Stress directions in the shallow part of the
1157 Hikurangi subduction zone, New Zealand, from the inversion of earthquake first motions.
1158 Geophysical Journal International, 142(2), 339–350. https://doi.org/10.1046/j.1365-
1159 246X.2000.00155.x
1160 McKinney, E., Marshall, J. S., Angenent, J., Hamel, J. E., Miller, C. N., Valenciano, J., ... &
1161 Litchfield, N. J. (2018, December). Coseismic Uplift and Coastal Emergence Along the
1162 Southern Hikurangi Margin, North Island, New Zealand. In AGU Fall Meeting
1163 Abstracts (Vol. 2018, pp. T51I-0285).
1164 Mochizuki, K., Sutherland, R., Henrys, S., Bassett, D., Van Avendonk, H., Arai, R., et al. (2019).
1165 Recycling of depleted continental mantle by subduction and plumes at the Hikurangi
1166 Plateau large igneous province, southwestern Pacific Ocean. Geology, 47(8), 795–798.
1167 https://doi.org/10.1130/g46250.1
1168 Mochizuki, K., Henrys, S., Haijima, D., Warren-Smith, E., & Fry, B. (2021). Seismicity and
1169 velocity structure in the vicinity of repeating slow slip earthquakes, northern Hikurangi
1170 subduction zone, New Zealand. Earth and Planetary Science Letters, 563, 116887.
1171 https://doi.org/10.1016/j.epsl.2021.116887
1172 Morgan, J. K., Solomon, E. A., Fagereng, A., Savage, H. M., Wang, M., Meneghini, F., Barnes,
1173 P. M., Bell, R. E., French, M. E., Bangs, N. L., Kitajima, H., Saffer, D. M., & Wallace, L.
1174 M. (2022). Seafloor overthrusting causes ductile fault deformation and fault sealing along

1175 the Northern Hikurangi Margin. *Earth and Planetary Science Letters*, *593*, 117651.
1176 https://doi.org/10.1016/j.epsl.2022.117651
1177 Mortimer, N., Hoernle, K., Hauff, F., Palin, J. M., Dunlap, W. J., Werner, R., & Faure, K.
1178 (2006). New constraints on the age and evolution of the Wishbone Ridge, southwest
1179 Pacific Cretaceous microplates, and Zealandia–West Antarctica breakup. Geology, 34(3),
1180 185-188.
1181 Nakai, J. S., Sheehan, A. F., Abercrombie, R. E., & Eberhart-Phillips, D. (2021). Near Trench
1182 3D Seismic Attenuation Offshore Northern Hikurangi Subduction Margin, North Island,
1183 New Zealand. *Journal of Geophysical Research: Solid Earth*, *126*(3), 1–20.
1184 https://doi.org/10.1029/2020JB020810
1185 Nicol, A., & Beavan, J. (2003). Shortening of an overriding plate and its implications for slip on
1186 a subduction thrust, central Hikurangi Margin, New Zealand. *Tectonics*, *22*(6), n/a-n/a.
1187 https://doi.org/10.1029/2003TC001521
1188 Okaya, D., Henrys, S., & Stern, T. (2002). Double-sided onshore-offshore seismic imaging of a
1189 plate boundary: "super-gathers" across South Island, New Zealand. *Tectonophysics*, *355*,
1190 247–263.
1191 Oleskevich, D. A., Hyndman, R. D., & Wang, K. (1999). The updip and downdip limits to great
1192 subduction earthquakes: Thermal and structural models of Cascadia, south Alaska, SW
1193 Japan, and Chile. Journal of Geophysical Research: Solid Earth, 104(B7), 14965–14991.
1194 https://doi.org/10.1029/1999JB900060
1195 Peltier, A., Hurst, T., Scott, B., & Cayol, V. (2009). Structures involved in the vertical
1196 deformation at Lake Taupo (New Zealand) between 1979 and 2007: New insights from
1197 numerical modelling. Journal of Volcanology and Geothermal Research, 181(3-4), 173-
1198 184.
1199 Plaza-Faverola, A., D. Klaeschen, P. Barnes, I. A. Pecher, S. Henrys, and J. Mountjoy (2012),
1200 Evolution of fluid expulsion and concentrated hydrate zones across the southern
1201 Hikurangi subduction Margin, New Zealand: An analysis from depth migrated seismic
1202 data, Geochem. Geophys. Geosyst., 13, Q08018, doi:10.1029/2012GC004228.
1203 Rait, G., F. Chanier, and D. W. Waters (1991), Landward- and seaward-directed thrusting
1204 accompanying the onset of subduction beneath New Zealand, Geology, 19(3), 230– 233,
1205 doi:10.1130/0091-7613(1991)019<0230:LASDTA>2.3.CO;2.
1206 Reyes, A. G., Christenson, B. W., & Faure, K. (2010). Sources of solutes and heat in low-
1207 enthalpy mineral waters and their relation to tectonic setting, New Zealand. Journal of
1208 Volcanology and Geothermal Research, 192(3–4), 117–141.
1209 https://doi.org/10.1016/j.jvolgeores.2010.02.015
1210 Reyes, A. G., Ellis, S. M., Christenson, B. W., and Henrys, S., 2022, Fluid flowrates and
1211 compositions and water–rock interaction in the Hikurangi margin forearc, New Zealand:
1212 Chemical Geology, p. 121169.
1213 Reyners, M., and S. Bannister (2007), Earthquakes triggered by slow slip at the plate interface in
1214 the Hikurangi subduction zone, New Zealand, Geophys. Res. Lett., 34, L14305, doi :
1215 10.1029/2007GL030511.
1216 Riefstahl, F., Gohl, K., Davy, B., & Barrett, R. (2020). Extent and Cessation of the Mid-
1217 Cretaceous Hikurangi Plateau Underthrusting: Impact on Global Plate Tectonics and the
1218 Submarine Chatham Rise. *Journal of Geophysical Research: Solid Earth*, *125*(8).
1219 https://doi.org/10.1029/2020JB019681

1220 Saffer, D. M., Wallace, L. M., Barnes, P. M., Pecher, I. A., Petronotis, K. E., LeVay, L. J., Bell,
1221 R. E., Crundwell, M. P., Engelmann de Oliveira, C. H., Fagereng, A., Fulton, P. M.,
1222 Greve, A., Harris, R. N., Hashimoto, Y., Hüpers, A., Ikari, M. J., Ito, Y., Kitajima, H.,
1223 Kutterolf, S., … Wu, H.-Y. (2019). *Expedition 372B/375 summary*. *372*(May).
1224 https://doi.org/10.14379/iodp.proc.372b375.101.2019
1225 Scherwath, M., Kopp, H., Flueh, E. R., Henrys, S. A., Sutherland, R., Stagpoole, V. M., Barker,
1226 D. H. N., Reyners, M. E., Bassett, D. G., Planert, L., & Dannowski, A. (2010). Fore-arc
1227 deformation and underplating at the northern Hikurangi margin, New Zealand. *Journal of*
1228 *Geophysical Research: Solid Earth*, *115*(6), 1–23. https://doi.org/10.1029/2009JB006645
1229 Shane, P., Sikes, E. L., & Guilderson, T. P. (2006). Tephra beds in deep-sea cores off northern
1230 New Zealand: Implications for the history of taupo volcanic zone, mayor island and white
1231 island volcanoes. Journal of Volcanology and Geothermal Research, 154(3–4), 276–290.
1232 https://doi.org/10.1016/j.jvolgeores.2006.03.021
1233 Shreedharan, S., Ikari, M., Wood, C., Saffer, D., Wallace, L., & Marone, C. (2022). Frictional
1234 and Lithological Controls on Shallow Slow Slip at the Northern Hikurangi Margin.
1235 *Geochemistry*, Geophysics, Geosystems, 23(2), 1–20.
1236 https://doi.org/10.1029/2021gc010107
1237 Smith, J. D., White, R. S., Avouac, J. P., & Bourne, S. (2020). Probabilistic earthquake locations
1238 of induced seismicity in the Groningen region, the Netherlands. Geophysical Journal
1239 International, 222(1), 507–516. https://doi.org/10.1093/GJI/GGAA179
1240 Stern, T., & Benson, A. (2011). Wide-angle seismic imaging beneath an andesitic arc: Central
1241 North Island, New Zealand. Journal of Geophysical Research: Solid Earth, 116(9), 1–26.
1242 https://doi.org/10.1029/2011JB008337
1243
1244 Stratford, W. R., & Stern, T. A. (2006). Crust and upper mantle structure of a continental
1245 backarc: Central North Island, New Zealand. Geophysical Journal International, 166(1),
1246 469–484. https://doi.org/10.1111/j.1365-246X.2006.02967.x
1247 Sun, T., Saffer, D., & Ellis, S. (2020). Mechanical and hydrological effects of seamount
1248 subduction on megathrust stress and slip. Nature Geoscience, 13(3), 249–255.
1249 https://doi.org/10.1038/s41561-020-0542-0
1250 Sutherland, R., Stagpoole, V., Uruski, C., Kennedy, C., Bassett, D., Henrys, S., Scherwath, M.,
1251 Kopp, H., Field, B., Toulmin, S., Barker, D., Bannister, S., Davey, F., Stern, T., & Flueh,
1252 E. R. (2009). Reactivation of tectonics, crustal underplating, and uplift after 60 Myr of
1253 passive subsidence, Raukumara Basin, Hikurangi-Kermadec fore arc, New Zealand:
1254 Implications for global growth and recycling of continents. *Tectonics*, *28*(5), 1–23.
1255 https://doi.org/10.1029/2008TC002356
1256 Taylor, B. (2006). The single largest oceanic plateau: Ontong Java-Manihiki-Hikurangi. Earth
1257 and Planetary Science Letters, 241(3–4), 372–380.
1258 https://doi.org/10.1016/j.epsl.2005.11.049
1259 Tichelaar, B. W., & Ruff, L. J. (1993). Depth of seismic coupling along subduction zones.
1260 *Journal of Geophysical Research*, *98*(B2), 2017–2037.
1261 https://doi.org/10.1029/92JB02045
1262 Van Avendonk, H. J. A., Shillington, D. J., Holbrook, W. S., & Hornbach, M. J. (2004).
1263 Inferring crustal structure in the Aleutian island arc from a sparse wide-angle seismic
1264 data set. Geochemistry, Geophysics, Geosystems, 5(8).
1265 https://doi.org/10.1029/2003GC000664

van de Lagemaat, S. H. A., Mering, J. A., & Kamp, P. J. J. (2022). Geochemistry of Syntectonic Carbonate Veins Within Late Cretaceous Turbidites, Hikurangi Margin (New Zealand): Implications for a Mid-Oligocene Age of Subduction Initiation. Geochemistry, Geophysics, Geosystems, 23(5). https://doi.org/10.1029/2021GC010125

Walcott, R. I., 1984, The kinematics of the plate boundary zone through New Zealand - a comparison of short-term and long-term deformations Geophysical Journal of the Royal Astronomical Society, v. 79, no. 2, p. 613-633.

Walcott, R. I. (1987), Geodetic strain and deformational history of the North Island of New Zealand in the late Cainozoic, Phil. Trans. roy. Soc. London, 321, 163-181.

Wallace, L. M. (2020). Slow Slip Events in New Zealand. Annual Review of Earth and Planetary Sciences, 48(1). https://doi.org/10.1146/annurev-earth-071719-055104

Wallace, L. M., & Beavan, J. (2010). Diverse slow slip behavior at the Hikurangi subduction margin, New Zealand. *Journal of Geophysical Research: Solid Earth*, *115*(12), 1–20. https://doi.org/10.1029/2010JB007717

Wallace, L. M., Beavan, J., McCaffrey, R., & Darby, D. (2004). Subduction zone coupling and tectonic block rotations in the North Island, New Zealand. *Journal of Geophysical Research: Solid Earth*, *109*(12), 1–21. https://doi.org/10.1029/2004JB003241

Wallace, L. M., Fagereng, Å., & Ellis, S. (2012). Upper plate tectonic stress state may influence interseismic coupling on subduction megathrusts. *Geology*, *40*(10), 895–898. https://doi.org/10.1130/G33373.1

Wallace, L. M., Reyners, M., Cochran, U., Bannister, S., Barnes, P. M., Berryman, K., Downes, G., Eberhart-Phillips, D., Fagereng, A., Ellis, S., Nicol, A., McCaffrey, R., Beavan, R. J., Henrys, S., Sutherland, R., Barker, D. H. N., Litchfield, N., Townend, J., Robinson, R., … Power, W. (2009). Characterizing the seismogenic zone of a major plate boundary subduction thrust: Hikurangi Margin, New Zealand. Geochemistry, Geophysics, Geosystems, 10(10). https://doi.org/10.1029/2009GC002610

Wallace, L. M., Barnes, P., Beavan, J., van Dissen, R., Litchfield, N., Mountjoy, J., et al. (2012). The kinematics of a transition from subduction to strike-slip: An example from the central New Zealand plate boundary. Journal of Geophysical Research, 117, B02405. https://doi.org/10.1029/2011JB008640

Wallace, L. M., Webb, S. C., Ito, Y., Mochizuki, K., Hino, R., Henrys, S., Schwartz, S. Y., & Sheehan, A. F. (2016). Slow slip near the trench at the Hikurangi subduction zone, New Zealand. Science, 352(6286), 701–704. https://doi.org/10.1126/science.aaf2349

Wang, K., Y. Hu, R. von Huene, and N. Kukowski (2010), Interplate earthquakes as a driver for shallow subduction erosion,Geology, 38(5), 431–434, doi:10.1130/G30597.1.

Wang, K., and S. L. Bilek (2014), Invited review paper: Fault creep caused by subduction of rough seafloor relief, Tectonophysics, 610, 1-24, doi:10.1016/j.tecto.2013.11.024.

Warren-Smith, E., Fry, B., Wallace, L. M., & Mochizuki, K. (2017). Near-source detection of near repeating seismicity triggered by shallow slow-slip, Northern Hikurangi, New Zealand.

Warren-Smith, E., Fry, B., Wallace, L., Chon, E., Henrys, S., Sheehan, A., Mochizuki, K., Schwartz, S., Webb, S., & Lebedev, S. (2019). Episodic stress and fluid pressure cycling in subducting oceanic crust during slow slip. *Nature Geoscience*, *12*(6), 475–481. https://doi.org/10.1038/s41561-019-0367-x

Williams, C. A., Eberhart-Phillips, D., Bannister, S., Barker, D. H. N., Henrys, S., Reyners, M., & Sutherland, R. (2013). Revised Interface Geometry for the Hikurangi Subduction

Zone, New Zealand. *Seismological Research Letters*, *84*(6), 1066–1073. https://doi.org/10.1785/0220130035

Wilson, C. J. N., Houghton, B. F., McWilliams, M. O., Lanphere, M. A., Weaver, S. D., & Briggs, R. M. (1995). Volcanic and structural evolution of Taupo Volcanic Zone, New Zealand: A review. Journal of Volcanology and Geothermal Research, 68(1–3), 1–28. https://doi. org/10.1016/0377- 0273(95)00006- G

Wilson, K., Litchfield, N., Berryman, K., and Little, T., 2007, Distribution, age, and uplift patterns of Pleistocene marine terraces of the northern Raukumara Peninsula, North Island, New Zealand: New Zealand Journal of Geology and Geophysics, v. 50, no. 3, p. 181-191.

Wood, R., & Davy, B. (1994). The Hikurangi Plateau. Marine Geology, 118(1–2), 153–173. https://doi.org/10.1016/0025-3227(94)90118-x

Yarce, J., Sheehan, A. F., Nakai, J. S., Schwartz, S. Y., Mochizuki, K., Savage, M. K., Wallace, L. M., Henrys, S. A., Webb, S. C., Ito, Y., Abercrombie, R. E., Fry, B., Shaddox, H., & Todd, E. K. (2019). Seismicity at the Northern Hikurangi Margin, New Zealand, and Investigation of the Potential Spatial and Temporal Relationships With a Shallow Slow Slip Event. *Journal of Geophysical Research: Solid Earth*, *124*(5), 4751–4766. https://doi.org/10.1029/2018JB017211

Yarce, J., Sheehan, A., Roecker, S., & Mochizuki, K. (2021). Seismic Velocity Heterogeneity of the Hikurangi Subduction Margin, New Zealand: Elevated Pore Pressures in a Region With Repeating Slow Slip Events. *Journal of Geophysical Research: Solid Earth*, *126*(5). https://doi.org/10.1029/2020JB021605

Zal, H. J., Jacobs, K., Savage, M. K., Yarce, J., Mroczek, S., Graham, K., Todd, E. K., Nakai, J., Iwasaki, Y., Sheehan, A., Mochizuki, K., Wallace, L., Schwartz, S., Webb, S., & Henrys, S. (2020). Temporal and spatial variations in seismic anisotropy and VP/VS ratios in a region of slow slip. *Earth and Planetary Science Letters*, *532*, 115970. https://doi.org/10.1016/j.epsl.2019.115970

Figures.

Figures

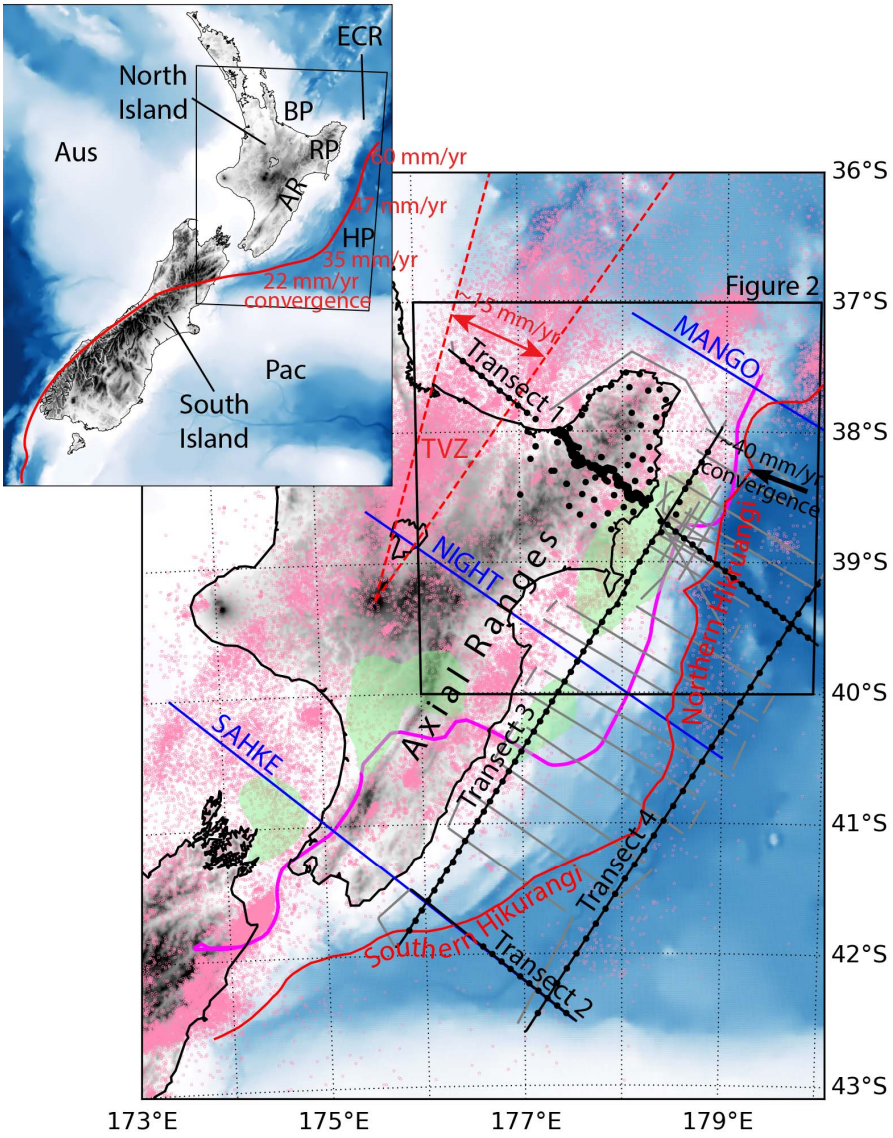

Figure 1: North Island, New Zealand, SHIRE setting. Rates of motion at the trench and in the backarc rift are from Wallace et al. (2004). Circles: GeoNet recorded seismicity M_W>2.5 from 2009 to 2019 (pink); SHIRE OBS and onshore stations (black). Lines: SHIRE transects (black); SHIRE MCS (gray); SAHKE, NIGHT, and MANGO transects (blue); Locked to creeping transition (magenta; Wallace et al., 2004); Hikurangi margin plate boundary (red); boundaries of the TVZ (dashed red). Green shaded regions show SSEs from Wallace et al. (2004). Boxed region shown in detail in Figure 2. AR: Axial Ranges; BP: Bay of Plenty; ECR: East Cape Ridge; HP: Hikurangi Plateau; RP: Raukumara Peninsula; TVZ: Taupo Volcanic Zone.

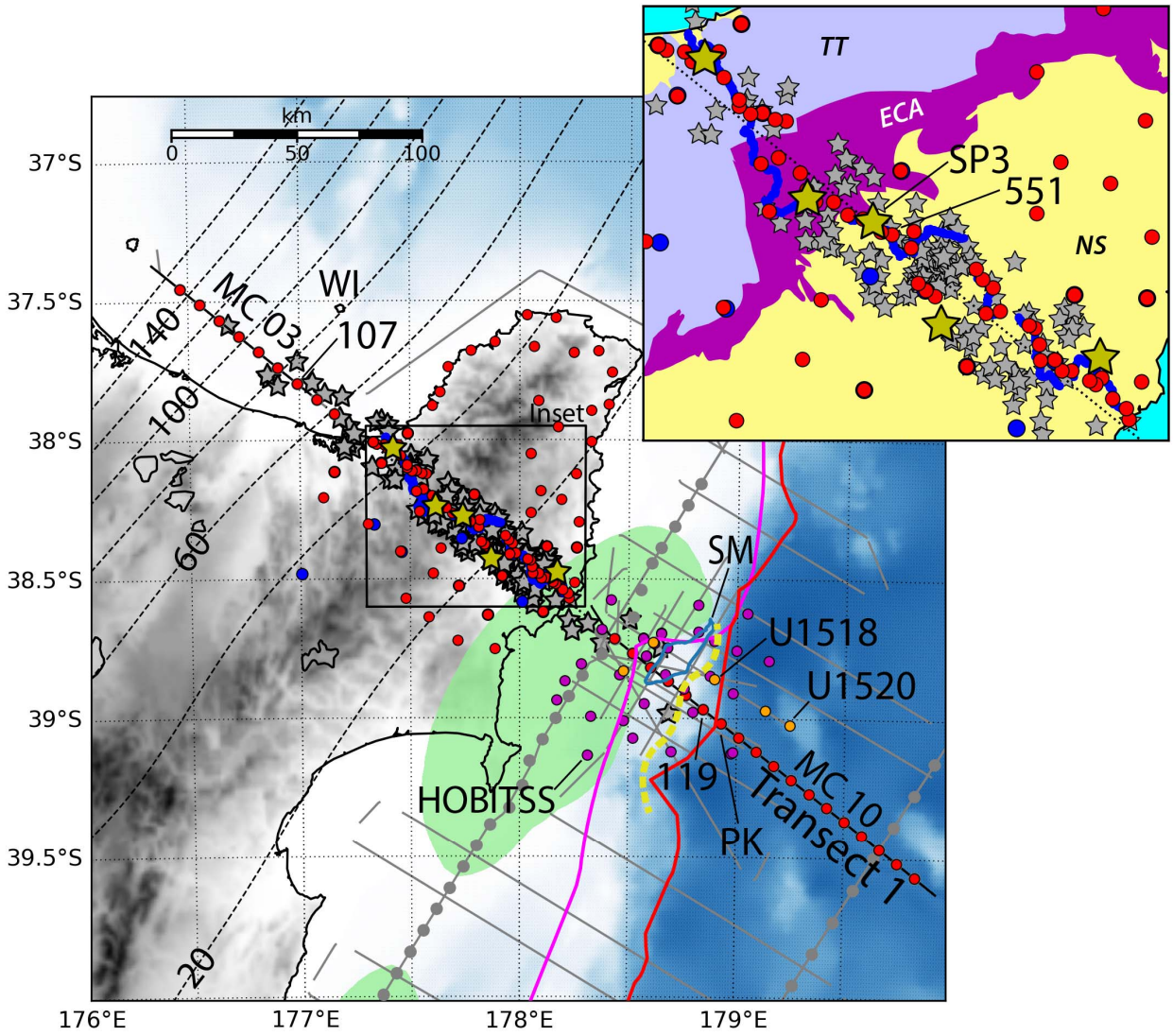

Figure 2: Raukumara Peninsula, North Island, New Zealand detail.SSEs from Wallace et al. (2004) shown in green. Subducting seamount outline from Barker et al. (2018) shown in blue. Lines: Hikurangi margin trench (red); slab depth contours (dashed black; Williams et al., 2013); Locked to creeping transition (magenta; Wallace et al., 2004); Contact between accretionary prism and deforming backstop (dashed yellow; Gase et al., 2021). Circles: SHIRE I stations (red); SHIRE II stations (blue); IODP drill sites (orange). Stars: SHIRE II explosion sources (yellow); SHIRE earthquake sources used in inversion (gray; see text). PK: Puke Knoll; WI: White Island; SM: seamount from Barker et al. (2018). SHIRE Transect 1 is the combined MC 10 and MC 03 reflection profiles; OBS sites; and onshore instrumentation from phases I and II. Inset: Detail of onshore Transect 1 deployment. Shaded onshore regions show simplified geologic units (TT: Torlesse Terrane; ECA: East Coast Allochthon; NS: Neogene sediments; Mazengarb & Spenden, 2000)

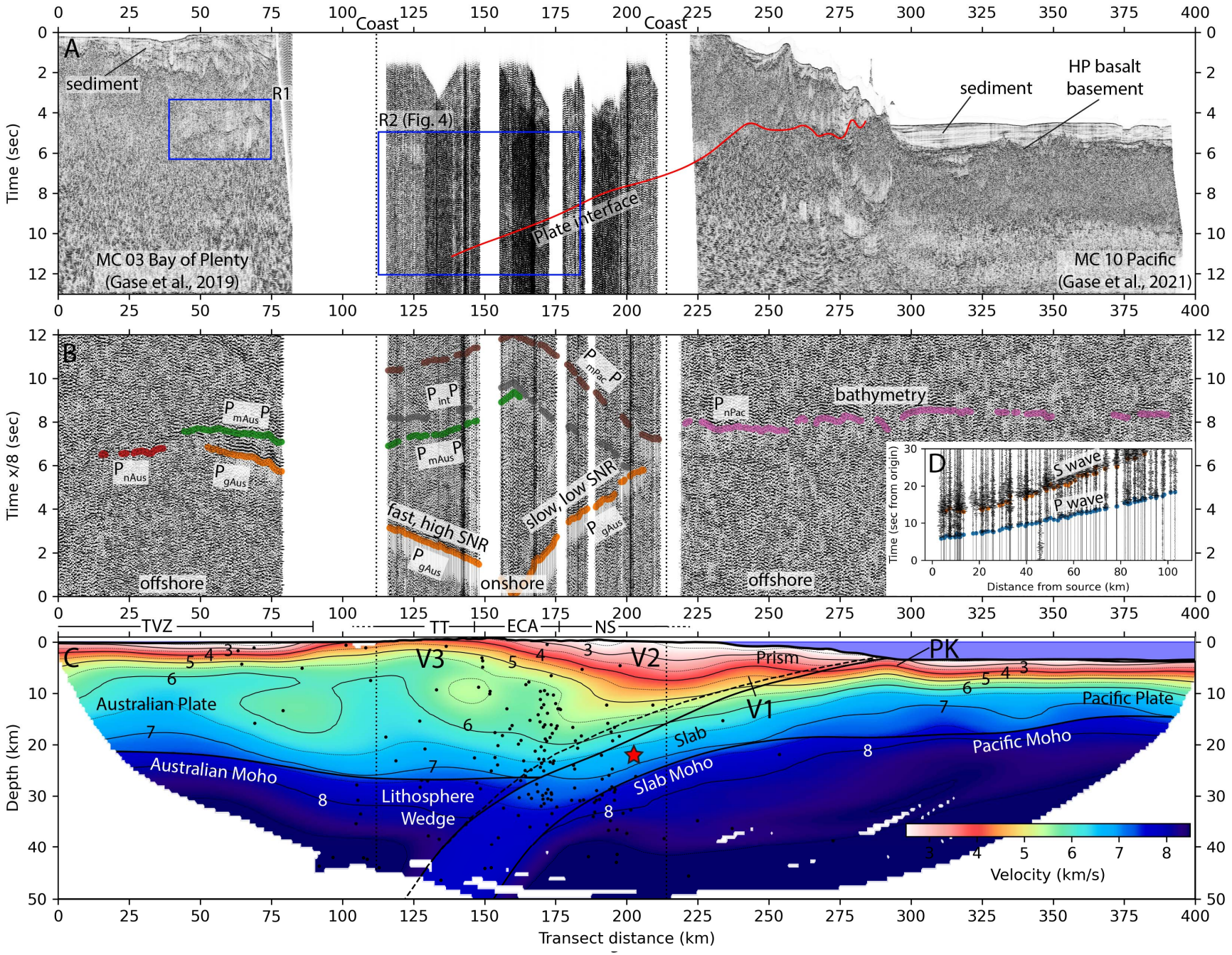
A
sediment
R1
R2 (Fig. 4)
Plate interface
Coast
Coast
HP basalt
basement
sediment
MC 03 Bay of Plenty
(Gase et al., 2019)
MC 10 Pacific
(Gase et al., 2021)
Time (sec)
B
P nAus
P mAus P
P gAus
P int P
P mPac P
P nPac
bathymetry
fast, high SNR
slow, low SNR
offshore
onshore
offshore
Time x/8 (sec)
D
S wave
P wave
Time (sec from origin)
Distance from source (km)
TVZ
TT
ECA
NS
C
V3
V2
V1
Prism
PK
Australian Plate
Pacific Plate
Australian Moho
Pacific Moho
Slab
Slab Moho
Lithosphere
Wedge
Velocity (km/s)
Depth (km)
Transect distance (km)

Figure 3: SHIRE Transect 1 data and resulting models. A: Reflection profiles from Bay of Plenty MCS (left panel, Gase et al., 2019), onshore low fold stacks, and Pacific MCS (right panel, Gase et al., 2021). Subduction interface observed in the Pacific from Gase et al. (2021) is observed within the onshore reflection profile. R1 is zone of reflectivity interpreted by Gase et al. (2019) as frozen sills. R2 is a zone of subparallel lower crustal reflectors above the Australian Moho extending from the plate interface to the west coast. B: Super-gather (Okaya et al., 2002) of onshore shot SP3 and OO station 551 (see Figure 2 for locations) plotted with a reduction velocity of 8.0 km/s. Crustal seismic phases P_{gAus}, $P_{mAus}P$, $P_{nPa}c$, $P_{mPa}cP$ are observed originating from shot 3, with phases identifiable nearly across the entire 400 km profile. Note that SP3 and OO 551 are ~3 km apart, shifting the *Pg-PmP-Pn* triplication point. C: P-wave velocities from active- and passive-source SHIRE T1 travel time data, masked where no ray coverage is present (Figure S1A). Lines: Calculated boundaries (solid black) and Williams et al. (2013) interface (dashed black). Earthquake data gather (red star) shown in E. See text for discussion of features V1, V2, and V3. PK: Puke Knoll. D: Earthquake gather recorded by the onshore SHIRE I array, highlighted in C.

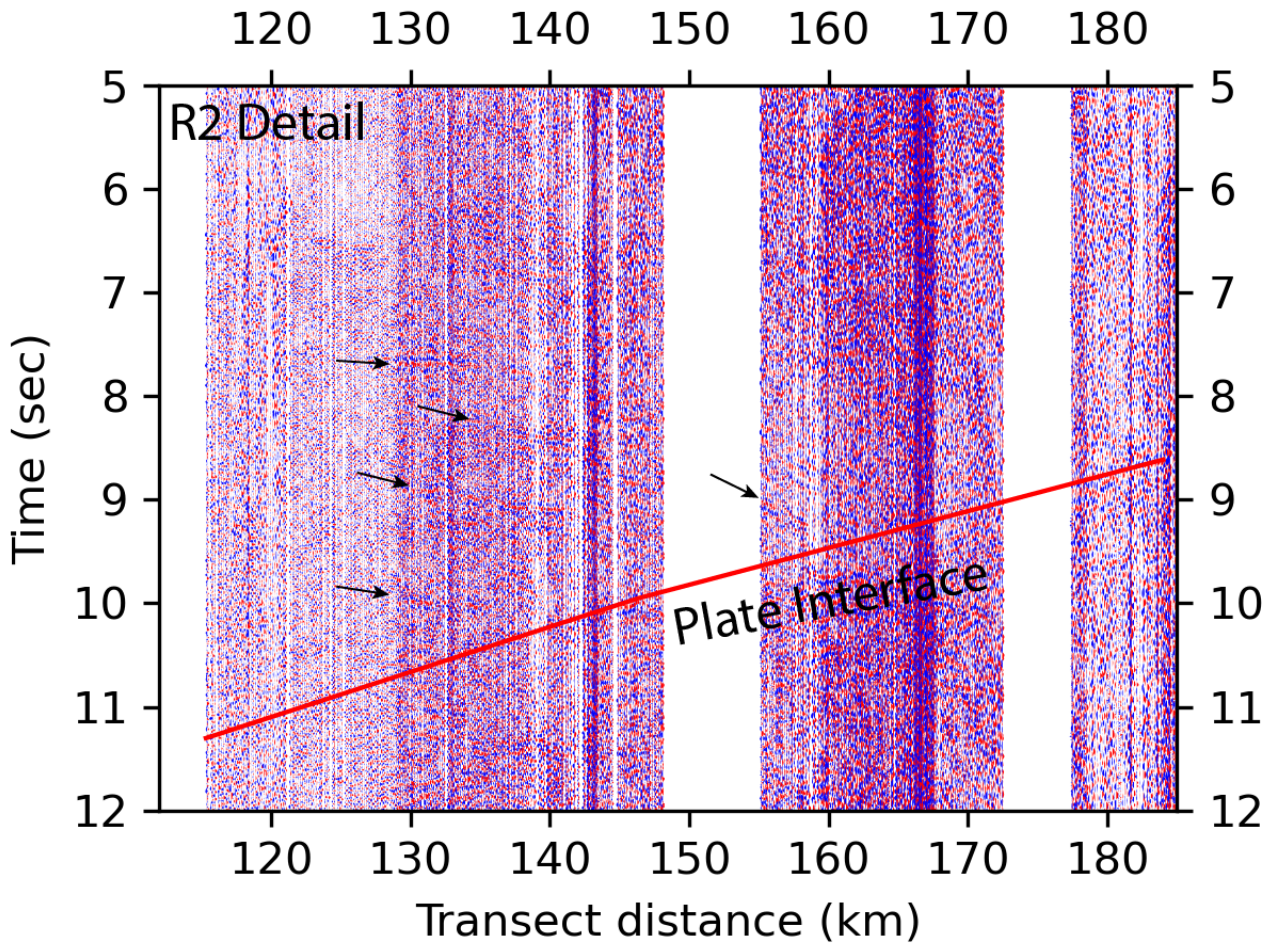

Figure 4: Interpreted detail of feature R2 from the CDP image in Figure 3A. Observed strong reflectors are highlighted with black arrows.

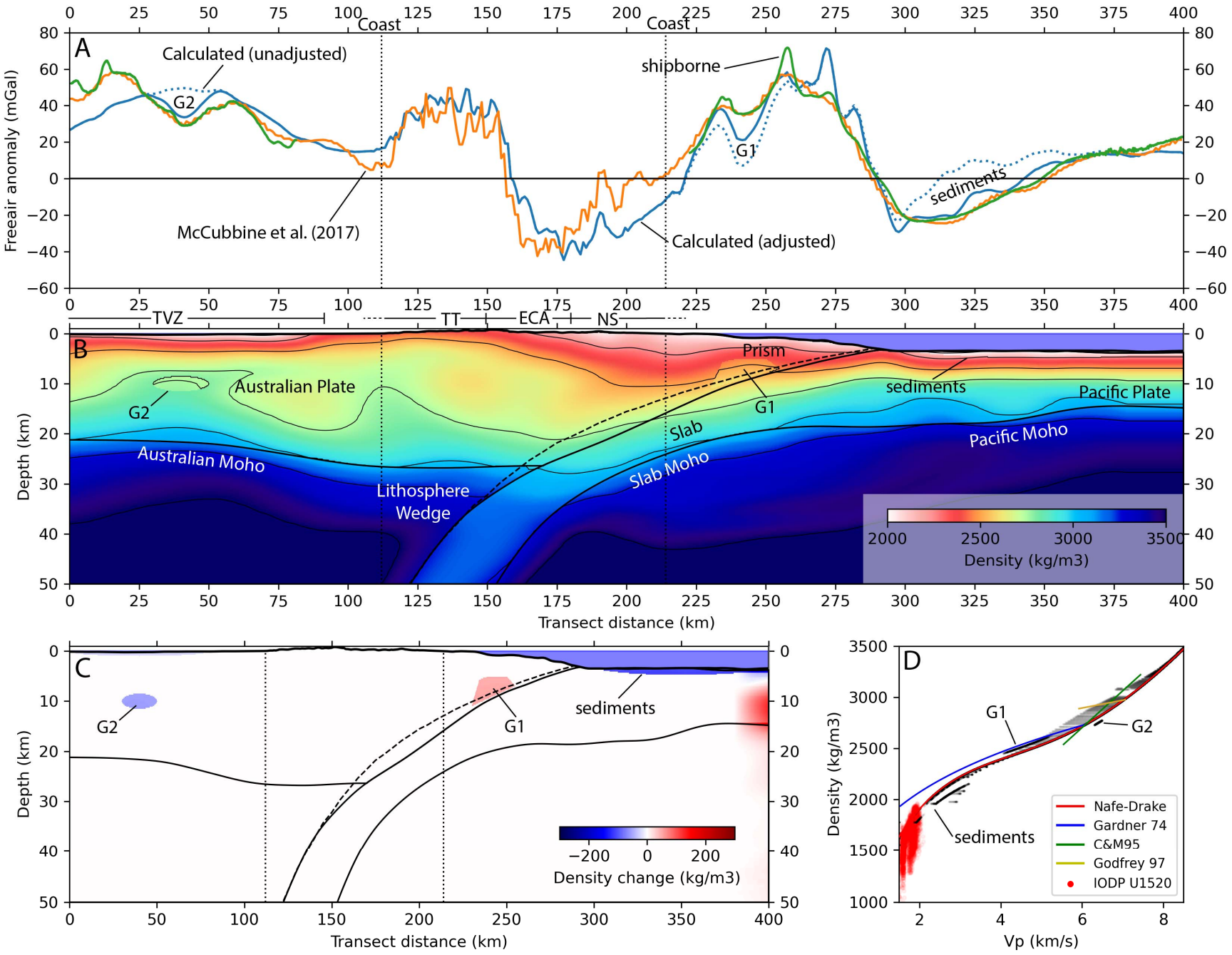
A
Calculated (unadjusted)
G2
McCubbine et al. (2017)
Coast
Coast
shipborne
G1
sediments
Calculated (adjusted)
Freeair anomaly (mGal)
TVZ
TT
ECA
NS
B
Australian Plate
G2
Australian Moho
Lithosphere
Wedge
Prism
G1
Slab
Slab Moho
sediments
Pacific Plate
Pacific Moho
2000
2500
3000
3500
Density (kg/m3)
Depth (km)
Transect distance (km)
C
G2
G1
sediments
−200
0
200
Density change (kg/m3)
Depth (km)
Transect distance (km)
D
G1
G2
sediments
Nafe-Drake
Gardner 74
C&M95
Godfrey 97
IODP U1520
Density (kg/m3)
Vp (km/s)

Figure 5: Density and free air gravity anomaly modelling of SHIRE T1. A: Anomalies calculated from unadjusted and manually adjusted SHIRE density model compared to SHIRE shipborne measured gravity and extracted profile from New Zealand-wide gravity anomaly model. B: 2-D density model converted from SHIRE P-wave velocities (Figure 3C) using Nafe-Drake relation and manually adjusted used to calculate the SHIRE free air gravity anomaly in A. C: Difference between adjusted and unadjusted density models. D: Velocity-density values calculated from SHIRE Vp (black circles) using the Nafe-Drake relation. Velocity-density measurements from IODP site U1520 (Saffer et al., 2019; see Figure 2 for location). Additional lithology-specific empirical relationships are shown: Sedimentary rocks (Gardner et al., 1974); crystalline rocks (Christensen & Mooney, 1995); and volcanics (Godfrey et al., 1997). See text for discussion of features G1 and G2.

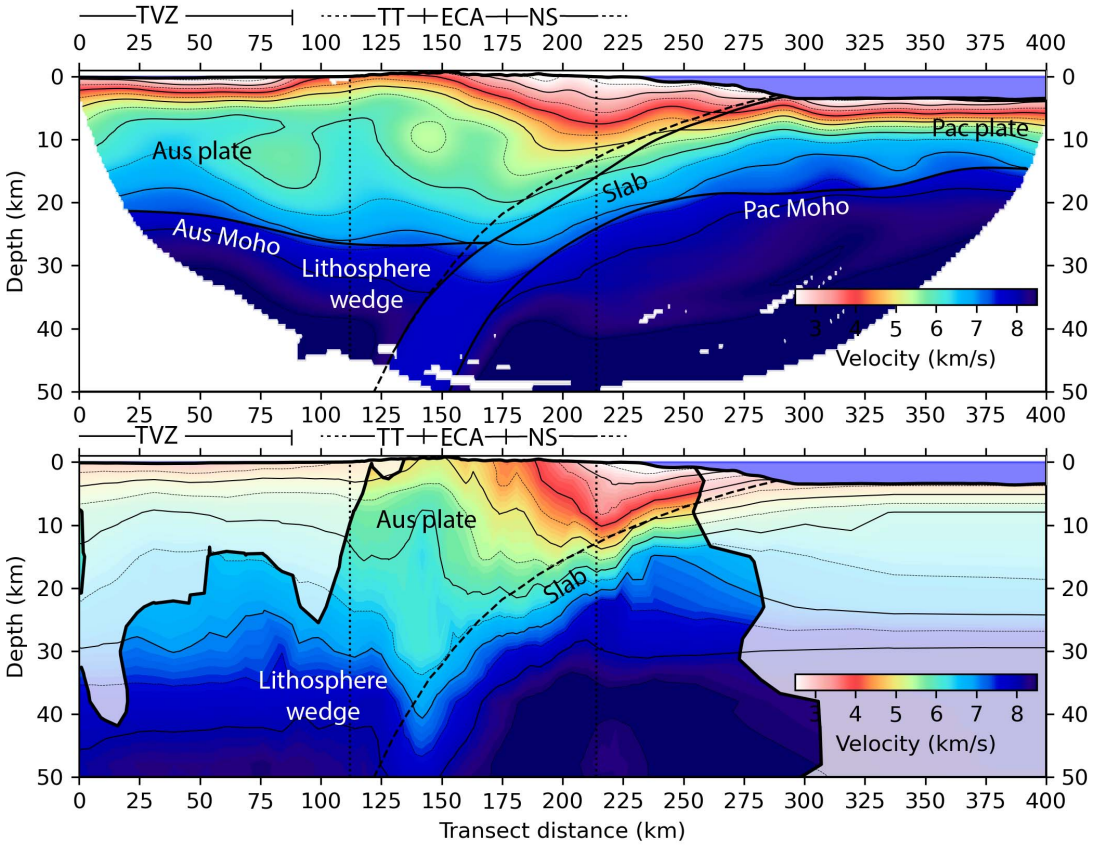

Figure 6: Comparison of SHIRE P-wave velocities (A) to extracted section from the 3-D regional earthquake P-wave model of Eberhart-Phillips et al. (2020; B). Both panels are plotted with the same color scale. B is masked where the resolution is considered unacceptable by Eberhart-Phillips et al. (2020; i.e., spread function >3.5). Lines: Model boundaries from Figure 3C (panel A; solid black); Williams et al. (2013) plate interface (panels A and B; dashed black).

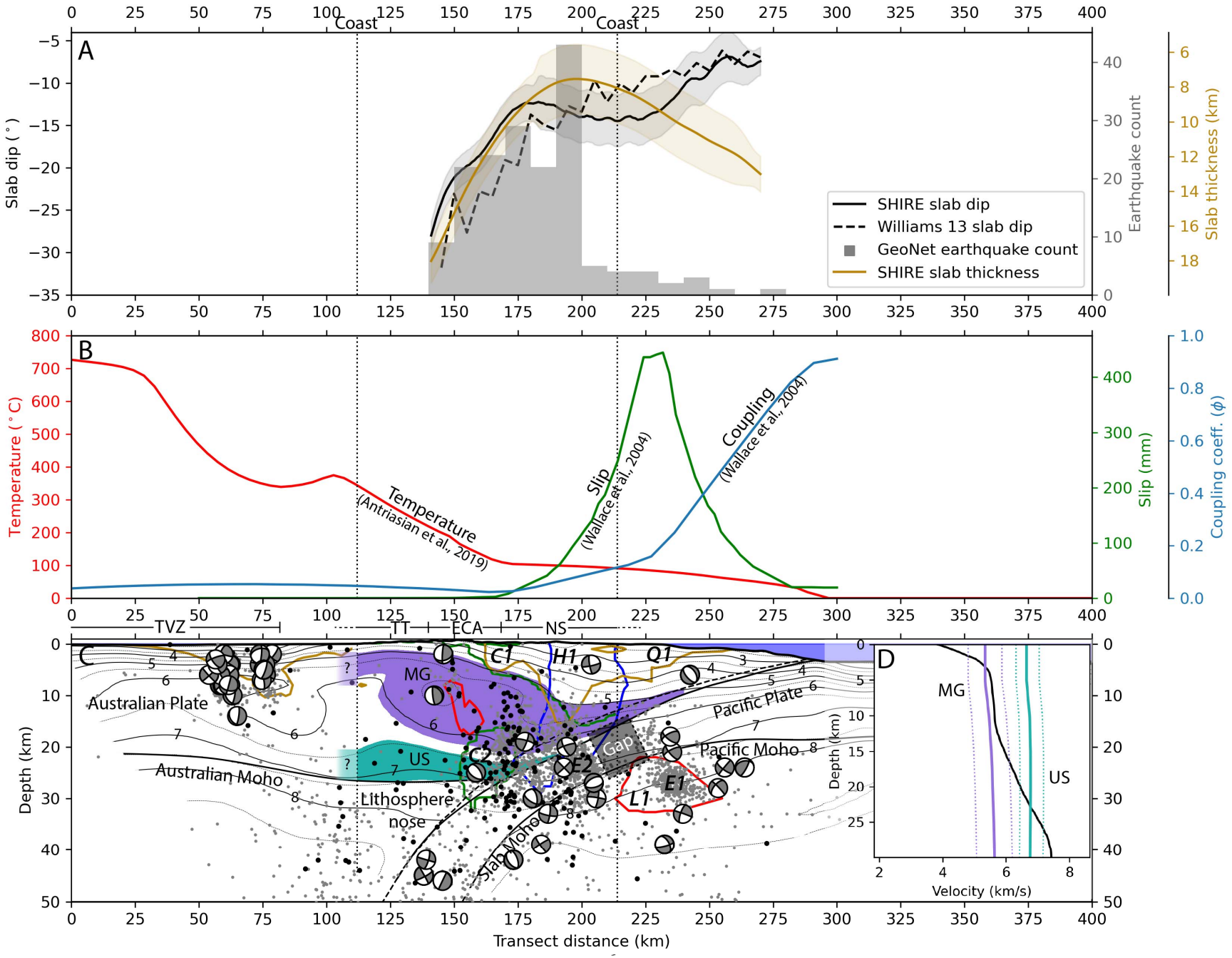
A
Coast
Coast
Slab dip (°)
Earthquake count
Slab thickness (km)
SHIRE slab dip
Williams 13 slab dip
GeoNet earthquake count
SHIRE slab thickness
B
Temperature (°C)
Slip (mm)
Coupling coeff. (ϕ)
Temperature
(Antriasian et al., 2019)
Slip
(Wallace et al., 2004)
Coupling
(Wallace et al., 2004)
TVZ
TT
ECA
NS
C
D
MG
US
C1
H1
Q1
C2
E2
E1
L1
Gap
Australian Plate
Australian Moho
Lithosphere
nose
Slab Moho
Pacific Plate
Pacific Moho
Depth (km)
Velocity (km/s)
Transect distance (km)

Figure 7: Interpretations of SHIRE T1 using Vp and outside datasets. A: Slab properties calculated from Figure 3C. B: Interface temperature, accumulated slow slip, and plate interface locking. C: Velocity contours and boundaries from Figure 3C. GeoNet focal mechanisms from 2003-2019 have been rotated into the plane of T1. Circles: SHIRE events used in inversion (black); GeoNet events from 2009-2019 within +/- 10 km of T1 (gray) with notable clusters of seismicity (E1, E2). Contours: resistivity <50 Ω-m (green; C1, C2; Heise et al., 2017); Vp/Vs >1.85 (blue; H1; Eberhart-Phillips et al., 2020); Vp/Vs <1.68 (red; L1; Eberhart-Phillips et al., 2020); Qp <250 (yellow; Q1; Eberhart-Phillips et al., 2020). Shaded regions: SHIRE Vp correlates with metagraywacke velocities (purple; MG; Christensen & Mooney, 1995); SHIRE Vp correlates with greenschist velocities (teal; US; Christensen & Mooney, 1995). D: Example 1-D velocity function from SHIRE Vp (C) compared to measurements from Christensen & Mooney (1995) used to shade MG and US in C. Lines: SHIRE 1-D function from transect distance 175 km (black); metagraywacke velocities (solid purple), greenschist velocities (solid teal), and rock velocity errors (dashed lines) from Christensen & Mooney (1995). TVZ: Taupo Volcanic Zone; TT: Torlesse Terrane; ECA: East Coast Allochthon; NS: Neogene Sediments; MG: Metagraywacke; US: Underplated (greenschist) sediments.

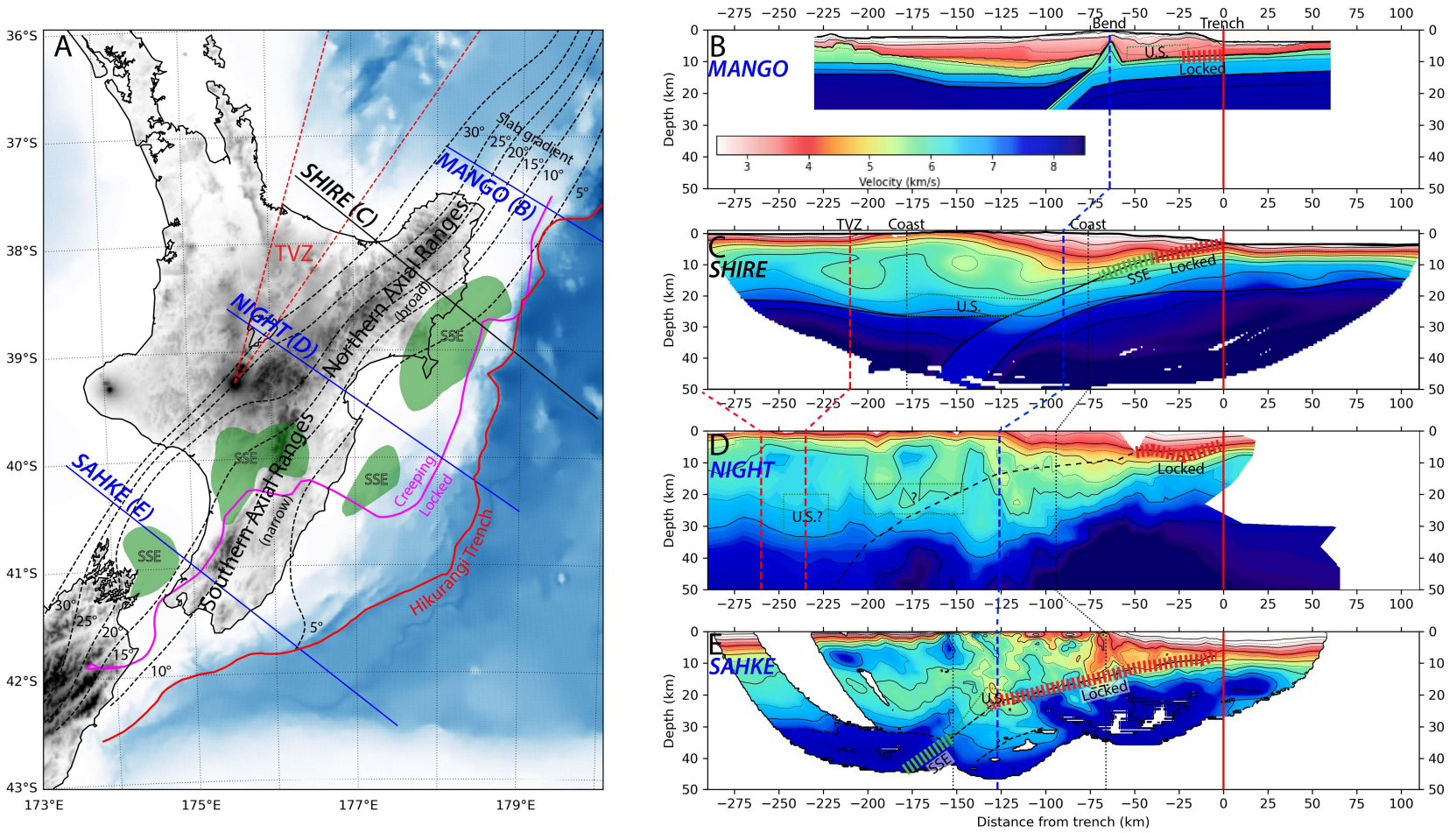

Figure 8: Along strike comparison of the Hikurangi margin. A: Relief map showing SAHKE (Henrys et al., 2013), NIGHT (Henrys et al., 2003), SHIRE, and MANGO (Scherwath et al., 2010) geophysical transects. SSE patches and locked-creeping transition from Wallace et al. (2004). Subduction interface gradient calculated from Williams et al. (2013) model (dashed black lines). C-E: Vp profiles from MANGO (B), SHIRE (C), NIGHT (D), and SAHKE (E) aligned with the trench and plotted with the same color scale. Locked plate interface (red dashed line) and locations of SSEs (green dashed line) are shown. Notable increase slab dip (blue dashed line) and extent of the TVZ (dashed red lines) are marked. Locations of underplated sediments (US) are delineated with green dashed

boxes. Note that the velocities shown in D are extracted from the 3-D model of Eberhart-Phillips et al. (2010) while the plate interface is from Henrys et al. (2003).